Journal of Directed Energy, **4**, Fall 2010, 32–70

Thermal Modeling of the Thin Disk Laser

Jochen Speiser*

German Aerospace Center, Institute of Technical Physics, Stuttgart, Germany

This paper discusses the needs and requirements of modeling the thin disk laser with a focus on thermal modeling. Results concerning high power extraction (>10 kW with one disk), including thermal behavior, stress, and thermal lenses are presented. Challenges of modeling high energy storage in a thin disk amplifier are discussed. An approach for modeling the influence of amplified spontaneous emission on the transient behavior of the inversion is described. In addition, an approach to find scaling limits due to amplified spontaneous emission is briefly described and results are presented.

KEYWORDS: Solid-state laser, Thin disk laser, Numerical modeling, Scaling limit

Nomenclature

α	absorption coefficient
α_0	absorption coefficient with zero excited ions
α_{th}	coefficient of thermal expansion
A_{ik}	area of interface between volume element i and k
$AR(\lambda,\vartheta)$	spectral and angular reflectivity of antireflective coating
ASE	amplified spontaneous emission
β_{λ}	spectral distribution of fluorescence
C	heat capacity
c_{00}	fundamental mode projection coefficient
c_{th}	thermal load parameter
c_{vac}	vacuum speed of light
δ_{ik}	distance between volume element i and k
e	Euler's number
E	amplitude of electrical field
E_{elast}	Young's modulus
Ei	exponential integral
E_p	pump power density
E_r	laser power density inside disk
ε_z	strain in z-direction
η_{abs}	pump absorption efficiency

*Corresponding author; e-mail: jochen.speiser@dlr.de.

η_{heat}	heat generation efficiency
f	frequency
f_{abs}	relative absorption on laser wavelength
$f_{abs}(\lambda, T)$	relative absorption on wavelength λ
$f_{em}(T)$	relative emission on pump wavelength
f_L	focal length of thermal lens
g	gain for one pass through disk
γ_{laser}	gain per length at laser wavelength (gain coefficient)
$g_\lambda(\vec{s})$	gain along vector $\vec{s}$ at wavelength λ
h	disk thickness
$\hbar$	reduced Planck constant
$H_{extractable}$	extractable energy per area
$HR(\lambda, \vartheta)$	spectral and angular reflectivity of high reflective coating
I_{heat}	heat load per area
k_B	Boltzmann constant
γ_λ	gain coefficient at wavelength λ
λ	wavelength
λ_{laser}	laser wavelength
λ_p	pump wavelength
λ_{th}	thermal conductivity (of laser material)
L_B	diffraction loss of fundamental mode
L_{int}	internal loss
M_p	number of pump beam passes through disk
M_r	number of laser beam passes through disk
n_0	refractive index at reference temperature
$\frac{\partial n}{\partial T}$	thermo-optical coefficient
N_0	volume density of laser ions
$\tilde{N}_0$	number of laser ions in a volume element
N_2	volume density of excited laser ions
$\tilde{N}_2$	number of excited laser ions in a volume element
N_{fluo}	number of initial probe photons for ASE calculation
n_{fluo}	integer representing amplification or loss of probe photons
Δn_{fluo}	net loss or amplification of probe photons in a volume element
ΔN_{ASE}	change of excited ion number in volume element due to ASE
ν	Poisson ratio
Ω	solid angle
φ	phase
$\Phi(r)$	optical phase distortion

Φ_r	number of laser photons per area and time (photon flux density)
$\Phi_{\lambda,\Omega}$	number of ASE photons per area and time (photon flux density)
P_{pump}	pump power
P_V	absorbed pump power in element
Q	source of excitation (e.g., absorbed pump photons per volume and time)
$\dot{q}_V$	heat load per volume
$\dot{q}_{Aik}$	the heat flux density through interface between volume element i and k
R	radius of disk
R_L	curvature
r_p	pump spot radius
$R_{th,cont}$	thermal resistance of contact layer between disk and heat sink
$R_{th,fl}$	effective thermal resistance for heat transfer to cooling fluid
$R_{th,HR}$	thermal resistance of heat sink
$R_{th,HS}$	thermal resistance of high-reflectivity coating
s	distance
$\vec{s}$	coordinate in disk
$\hat{s}$	direction
$\sigma_{abs(T)}$	absorption cross-section at pump wavelength
$\sigma_{em(\lambda,T)}$	emission cross-section at wavelength λ and temperature T
$\sigma_{em,laser}$	emission cross-section at laser wavelength
T	temperature
T_0	temperature at cooled face of disk
τ	fluorescence lifetime
τ_{ASE}	reduced lifetime of excited ions due to ASE
T_{av}	average temperature in disk
T_{cool}	temperature of cooling fluid
T_i	temperature of volume element i
T_k	temperature of neighboring volume element to element i
$T_{\max}$	maximum temperature in disk
T_{oc}	transmission of output coupler
V_i	volume of volume element i
w	mode radius
z_0	displacement of HR side of disk
Z_1	partition function of lower laser level
Z_2	partition function of upper laser level
z_{PD}	penetration depth for a harmonic heat source

1. Introduction

Numerical modeling is an essential tool for designing thin disk lasers. Consequently, early work on thin disk lasers was supported by numerical modeling (cf., e.g., Voss et al.[1] and Giesen et al.[2]). From these first steps, a more sophisticated model was derived (for description, see Contag et al. (1999)[3] and Contag (2002)[4]). This numerical model was optimized for Yb:YAG. Models for other disk materials were developed in a similar fashion. Kemp et al.[5] provide a review for neodymium-doped materials.

A large portion of the modeling work is devoted to thermal modeling. This is due to the fact that four main topics of thin disk laser design are closely related to thermal modeling: thermal management, mechanical strength, laser dynamics of quasi-three-level materials, and thermal lensing.

The basic idea of the thin disk design is that thermal management is much easier if heat is removed along the smallest dimension of the active laser medium. Thermal modeling is necessary to identify optimization possibilities of contact materials and heat sink material, or to determine whether cooling the disk from two sides is useful.

An immediate result of reduced thickness of the thin disk is limited mechanical strength if it is used without supporting structures. In addition, typically only a cylindrical volume inside the disk is pumped, not the whole disk, and the pump power is not necessarily distributed homogeneously inside the pumped volume. The resulting temperature differences inside the disk will lead to thermally induced stress, which, if strong enough, may destroy the disk. For an unsupported disk, this strongly limits power, but if supporting structures are added, thermal modeling of such structures is required as well. As these structures will be part of thermal management, they will show thermally induced stress and typically some deformation due to thermal gradients. Therefore, mechanical modeling of the thin disk laser is required to resolve mechanical strength and mechanical behavior issues.

Another important fact about the thin disk laser is that the typical and most beneficial active materials are quasi-three-level materials, that is, materials with significant thermal population of the lower laser level. The gain as well as pump absorption of these materials show strong temperature dependence. Therefore, each calculation of absorption and amplification requires adequate knowledge of the temperature distribution inside the disk. This is especially important for optimization of parameters such as thickness or doping concentration of the active medium. But it is also necessary, for example, to determine whether an experimental result achieved on a low power level can be easily scaled to higher power levels.

The fourth important issue is the thermal lens of the thin disk laser. This lens is small, but it is not negligible, especially for high power, high brightness operation. Due to the scaling behavior, high power means large pumped areas and therefore large mode diameters to reach high beam quality. This results in a high sensitivity to thermal lensing. The thermal lens is composed of two different contributions: first is the change in length of the optical path through the active medium (and maybe through some additional structures inside the resonator) due to temperature dependence of the refractive index and the thermal expansion of the material, and second, the mechanical deformation of the whole structure of heat sink, thin disk, and supporting elements due to thermally induced stress.

In Section 2, some basic properties for the modeling and also some basic considerations on thermal management are discussed. In Section 3, a spatially resolved model for absorption,

gain, inversion, and temperature is described. In Section 4 some results of FEM-based thermal and mechanical modeling are presented, which are further analyzed concerning the thermal lens in Section 5. In Section 6, some challenges for pulsed operation, especially in the case of quasi-cw pumping are discussed. In Section 7, some results on scaling limits are presented.

2. Basic Properties

2.1. Heat source

To perform thermal modeling, the most important questions are the amount and distribution of the thermal load in the thin disk laser. Several different contributions are identified. First, each absorbed pump photon excites a laser ion. This excitation will be transformed either to fluorescence or stimulated emission or it will be lost by nonradiative decay processes. The energy difference will be transformed to heat. The heat distribution is dominated by the distribution of absorbed pump power and can be calculated based on a model of the inversion. A second heat source can be the absorption of pump or laser radiation by the host material or by the interfaces of the thin disk. But these absorptions must be very small in order to enable the operation of the thin disk laser (due to the small gain) and can be neglected in most situations.

A heat source that is a bit more complex is the interaction with the fluorescence, and especially with the amplified spontaneous emission (ASE). In a simple approach, the fluorescence will be reflected, transmitted, or absorbed at the various interfaces of the thin disk, depending on design details. A "guiding" behavior is expected for the fluorescence in the plane of the disk due to the high reflective (HR) coating at the back side and the total internal reflection at the front side. This will at least result in heat generation behind the HR-coated back side, which will always have some transmission at large angles. A more elaborate approach also has to take into account that the fluorescence (especially "guided" fluorescence) is absorbed or amplified in the disk, generating an additional heat source outside the pumped volume. In addition, this absorption and amplification will strongly interact with the inversion distribution and can strongly influence the possible gain and output power.

2.2. Equation of motion

The fundamental equation of motion for the density of excited ions is

$$\dot{N}_2 = Q - \frac{N_2}{\tau} - \gamma_{laser}\Phi_r \tag{1}$$

with Q representing the source (e.g., the absorbed pump photons per volume and time), τ the lifetime fluorescence, γ_{laser} the gain per length at the laser wavelength (gain coefficient), and Φ_r the number of laser photons per area and time (photon flux density).

The typical laser material for the thin disk setup is Yb:YAG, at room temperature a quasi-three-level laser material; that is, the lower laser level is thermally populated. For a given density of excited ions N_2, density of laser ions N_0, and emission cross-section $\sigma_{em}(\lambda,T)$ at wavelength λ, the gain coefficient follows:

$$\gamma_\lambda = \sigma_{em}(\lambda,T)\left(1+f_{abs}(\lambda,T)\right)N_2 - \sigma_{em}(\lambda,T)f_{abs}(\lambda,T)N_0 \tag{2}$$

with

$$f_{abs}(\lambda,T) = \frac{Z_2(T)}{Z_1(T)}\exp\left(\frac{2\pi\hbar c_{vac}}{\lambda k_B T}\right) \tag{3}$$

and Z_1 and Z_2 the partition functions of the lower and upper laser levels, respectively.

Similarly, one can also calculate the absorption coefficient for a given absorption cross-section $\sigma_{abs}(T)$ at the pump wavelength λ_p as follows:

$$\alpha = \sigma_{abs}(T)N_0 - \sigma_{abs}(T)\left(1+f_{em}(T)\right)N_2 \tag{4}$$

with

$$f_{em}(T) = \frac{Z_1(T)}{Z_2(T)}\exp\left(-\frac{2\pi\hbar c_{vac}}{\lambda_p k_B T}\right) \tag{5}$$

With this absorption coefficient, thickness of the disk h and pump power density E_p, we can calculate the number of absorbed pump photons per volume and time as follows,

$$Q = \frac{E_p\lambda_p}{2\pi\hbar c_{vac}}\frac{\left(1-\exp\left(-\alpha h M_p\right)\right)}{h} \tag{6}$$

if we use M_p pump beam passes through the disk.

We also calculate the gain at the laser wavelength for one pass through the disk

$$g = h\left(\sigma_{em,laser}\left(1+f_{abs}(T)\right)N_2 - \sigma_{em,laser}f_{abs}(T)N_0\right) \tag{7}$$

As energy extraction is only possible if $g > 0$, we can similarly define the maximum extractable energy per area as follows:

$$H_{extractable} = \frac{2\pi\hbar c_{vac}}{\lambda_{laser}}h\left(\left(1+f_{abs}(T)\right)N_2 - f_{abs}(T)N_0\right) \tag{8}$$

These formulas ensure the correct handling of thermal population, bleaching, and saturation effects.

2.3. Basic Thermal Modeling

Due to the thin disk design, that is, that one face is cooled and the thickness is small compared to the lateral dimensions of the active area, it is possible to use one-dimensional heat conduction as a first assumption. If we apply pump power P_{pump} on a pump spot with radius r_p with an absorption efficiency η_{abs} and a heat generation η_{heat} to disk with thickness h, made of a material with thermal conductivity λ_{th}, the heat load per area is

$$I_{heat} = \frac{P_{pump}\eta_{abs}\eta_{heat}}{\pi r_p^2} \tag{9}$$

This heat load will result in a parabolic temperature profile inside the disk,

$$T(z) = T_0 + I_{heat}\frac{h}{\lambda_{th}}\left(\frac{z}{h} - \frac{1}{2}\frac{z^2}{h^2}\right) \tag{10}$$

with $z = 0$ representing the cooled face of the disk at temperature T_0.

The maximum temperature will be

$$T_{\max} = T_0 + \frac{1}{2} I_{heat}\frac{h}{\lambda_{th}} \tag{11}$$

and the average temperature,

$$T_{av} = T_0 + \frac{1}{3} I_{heat}\frac{h}{\lambda_{th}} \tag{12}$$

For a classic disk mounted on a heat sink, we have to consider also the heat resistance of the HR coating $R_{th,HR}$, the heat resistance of the "contact" layer (indium, solder, or glue) $R_{th,cont}$, and of the heat sink $R_{th,HS}$. In addition, there will be a temperature difference between the back side of the heat sink and the cooling fluid, which can be represented by a heat resistance $R_{th,fl}$. Therefore, the maximum temperature can be expressed as

$$T_{\max} = T_{cool} + I_{heat}\cdot\left(\frac{1}{2}\frac{h}{\lambda_{th}} + R_{th,HR} + R_{th,cont} + R_{th,HS} + R_{th,fl}\right) \tag{13}$$

with T_{cool} the temperature of the cooling fluid.

This is a steady-state point of view; the transient behavior of the temperature in thin disk lasers is typically not considered. Based on simple considerations, we can at least find the range of validity of these steady-state formulas. The so-called "penetration depth" z_{PD} of a harmonic heat source with oscillation frequency f on the surface of a semi-infinite solid can be found in most textbooks on heat transfer processes (e.g., Baehr and Stephan[6]):

$$z_{PD} = \sqrt{\frac{\lambda_{th}}{\pi\rho C f}} \tag{14}$$

with λ_{th} the thermal conductivity, ρ the density, and C the heat capacity. At z_{PD}, the amplitude of the oscillation is reduced by $1/e$. Typical time constants in the laser are the photon lifetime, which is for a long resonator (3-m resonator length) with 4% total losses at roughly 500 ns (i.e., 2 MHz); the relaxation-oscillation frequency, which we can expect to be about 25 kHz for a long-cavity, Yb:YAG thin-disk laser; and finally, the fluorescence lifetime, roughly 1 ms.

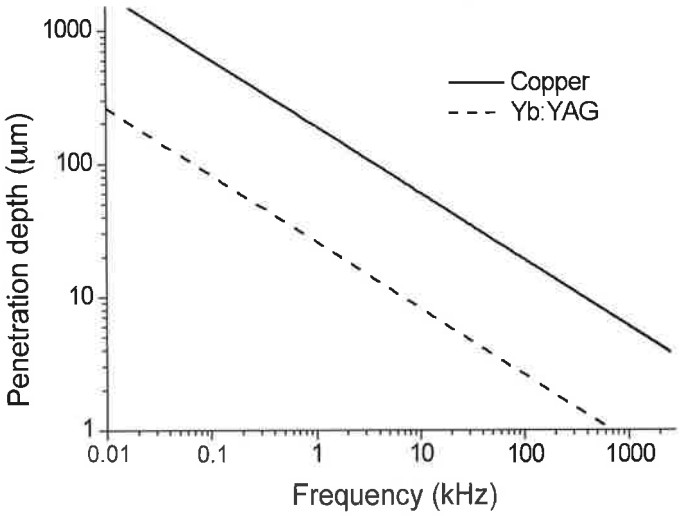

Fig. 1. Penetration depth for copper and Yb:YAG.

As depicted in Fig. 1, the penetration depth is only a few micrometers in Yb:YAG and less than 100 µm in copper for frequencies of more than 10 kHz. We can expect that for continuous pumping, the temperature distribution inside the disk and the cooling system will show only very small deviations from the steady state after a few milliseconds. A time-resolved temperature model will be necessary only for quasi-cw pumping with frequencies smaller than 100 Hz.

The assumption of one-dimensional heat conduction is suitable for some optimization. Especially for large pump spots, it describes the temperature rise in the center of the disk with good accuracy (e.g., Larionov[7] shows that the radial heat flow is less than 10% of the axial heat flow for a pump spot diameter larger than 12 times the disk thickness). But neither the exact temperature distribution inside the disk nor the heat spreading effects in the heat sink or in a transparent heat spreader can be described with this method. These effects are of special interest for calculations of stress and deformation.

In early publications on the thin disk design (Voss et al.[1] and Giesen et al.[2]), calculations of the temperature distribution in the disk using finite element methods (FEM) were presented. The first patent application[8] also contains consideration on how to influence the temperature distribution by radially nonuniform cooling, which was also confirmed by FEM calculations. In Cousins,[9] temperature calculations for very short, face-cooled laser rods are presented, based on analytical integration of the three-dimensional heat equation (with radial symmetry) and on FEM calculations. All these calculations are restricted to the active element, that is, the thin disk or short rod, and do not consider a heat sink. This is of special importance, as these publications also deal with the calculation of deformation and stress, which are strongly influenced by the interaction with heat sink/heat spreader components as will be discussed later.

Kemp et al.[5] provide a comprehensive overview of modeling four-level, thin disk lasers, which also includes detailed FEM analysis of various mounting designs, including thermal

lens calculations like those in Sections 4 and 5 of this paper. Kemp et al.[5] do not take into account the mechanical influence of the heat sink.

3. Coupled Modeling of Absorption, Temperature, and Laser Amplification

As previously mentioned, Yb:YAG shows significant temperature-dependent reabsorption of laser radiation. In the thin disk design, it is operated at a comparably high inversion level, resulting in significant reduction of the pump absorption. Consequently, the coupling between the differential equations of pump absorption, laser amplification, inversion, and temperature must not be neglected.

Over the last two decades, a model was developed to account for this coupling. The first publication was released in 1997[10]; more details and correlations with experimental results are given in Contag et al. (1999 and 2000)[3,11]; and a complete description appears in Contag (2002).[4] A very important design feature of the thin disk laser was developed based on this model: the immense benefit for system performance from higher numbers of pump beam passes. As an illustration, it was proven numerically and experimentally that doubling the number of pump beam passes from 8 to 16 (with optimized thickness and doping level in both cases) gives the same increase in efficiency as reducing the cooling fluid temperature from 15 °C to –25 °C (e.g., Contag et al.[3]).

The core idea of the coupled model is to perform an iterative calculation as follows: (1) pump absorption, (2) temperature distribution based on the stokes defect as the heat source, (3) inversion density and laser output power, and (4) absorption, but now with the changed temperature distribution and taking into account the bleaching of absorption due to the calculated inversion. This is repeated until a convergence criterion (typically the change of output power compared to the previous iteration) is reached. Models with a very similar approach have been presented recently by Najafi et al.[12] and Javadi-Dashcan.[13]

Figure 2 shows the flow chart of this model. In order to realize a spatially resolved model, the disk is discretized in finite elements in radial, azimuthal, and axial directions. In addition, for the calculation of the temperature distribution, the heat sink and the solder layer are discretized similarly. The HR coating and the heat transfer to the cooling fluid are represented by appropriate heat resistance values.

The equation of motion, derived from Eq. (1) of the number $\tilde{N}_2$ of excited Yb^{3+} ions in each element, is described by the following equation for each element:

$$\frac{\partial \tilde{N}_2}{\partial t} = \frac{\lambda_p P_V}{2\pi\hbar c_{vac}} + \frac{\lambda_l M_r E_r}{2\pi\hbar c_{vac}} \sigma_{em,laser} \left(\tilde{N}_0 f_{abs} - \tilde{N}_2 \left(1 + f_{abs}\right) \right) - \frac{\tilde{N}_2}{\sigma} \tag{15}$$

with P_V representing the absorbed pump power in the element, and E_r the laser power density inside the thin disk.

The calculation is initialized by calculating the absorbed pump power. In order to do this, a Monte-Carlo ray tracing method is used, following each photon from the source (e.g., the end of the fiber in the case of a fiber-coupled pump diode) through the complete system. For the calculation, starting parameters can be set according to real measurements (wavelength distribution, power density distribution, numerical aperture). The program determines for each photon in which segment of the disk the absorption takes place or

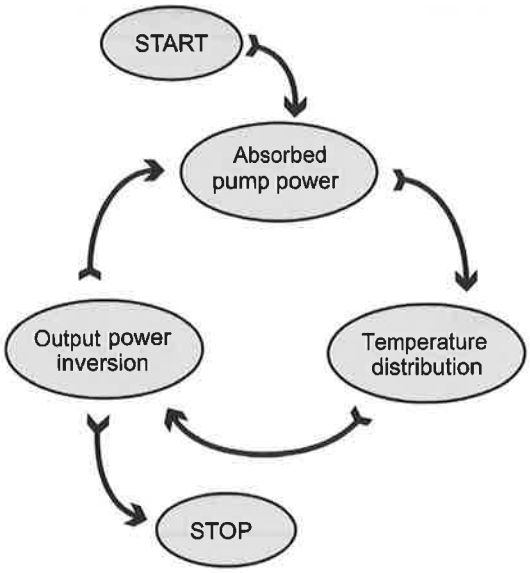

Fig. 2. Flow chart of the coupled modeling of absorption, temperature, and laser amplification.

whether the photon is lost for the lasing process (absorption in optical components or at apertures or whether the photon is not absorbed in all the pump beam passes through the disk). The absorption coefficient is described by

$$\alpha = \alpha_0 \cdot \left(1 - \left(1 + f_{em} \exp\left(-\frac{2\pi\hbar c_{vac}}{\lambda_p k_B T}\right)\right)\frac{\tilde{N}_2}{\tilde{N}_0}\right) \tag{16}$$

taking into account the bleaching of the absorption caused by the depopulation of the lower pump level and the population of the upper pump level.

The calculation method will be illustrated with some results from a sample configuration. The parameters are listed in Table 1. Fig. 3 shows the radial distribution of the absorbed pump power in this initial step for a sample configuration.

The next step is calculating the temperature distribution in the disk based on the steady-state heat conduction equation

$$\lambda_{th} \Delta T = \dot{q}_V \tag{17}$$

with the Stokes defect as heat source $\dot{q}_V$. This partial differential equation is solved iteratively using

$$\sum_k \lambda_{th} \frac{T_k - T_i}{\delta_{ik}} A_{ik} = \dot{q}_V V_i + \sum_k \dot{q}_{Aik} A_{ik} \tag{18}$$

Table 1. Sample configuration parameters

Thickness h of the Yb:YAG	180 μm
Diameter R	60 mm
Thermal resistance of HR coating $T_{th,HR}$	14.5 K/(Wmm²)
Thickness of solder	30 μm
Thickness of CuW	1.5 mm
Heat transmission resistance between heat sink and cooling fluid $R_{th,fl}$	3 K/(Wmm²)
Temperature of cooling fluid T_{cool}	15 °C
Number of pump passes	24
Loss in pump optic per pass	0.1%
Pump profile	Top hat
Pump power	25.6 kW
Pump spot diameter r_p	About 22 mm
Number of passes through disk	4
Transmission of outcoupling mirror	4%
Additional internal loss in resonator	0.2%

for each volume element V_i, with T_k the temperatures of the neighbor elements, δ_{ik} the distance to the neighbor elements, A_{ik} the interface area between the corresponding volume elements, and $\dot{q}_{Aik}$ the heat flux density through the interface. This system of linear equations is solved iteratively by a Gauss-Seidel method. Fig. 4 shows the heat generation during the initial step for this sample configuration, and Fig. 5 shows the calculated temperature distribution.

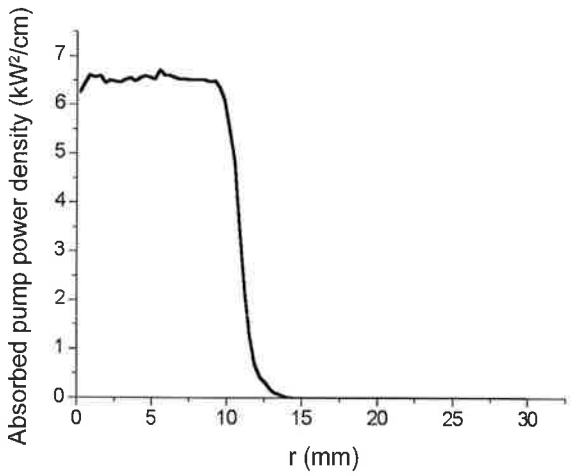

Fig. 3. Radial distribution of absorbed pump power after initial step of iteration (step 0): 9% Yb:YAG, thickness 180 μm, diameter 60 mm, 24 pump passes, pump spot diameter 22 mm, and pump power 25.6 kW.

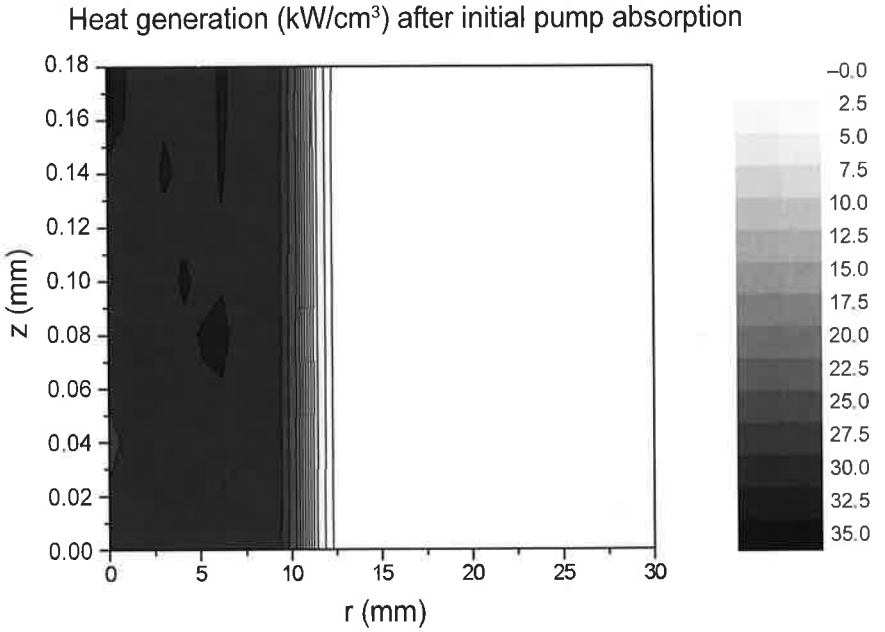

Fig. 4. Distribution of heat generation after initial step of iteration (step 0) 9% Yb:YAG, thickness 180 μm, diameter 60 mm, 24 pump passes, pump spot diameter 22 mm, and pump power 25.6 kW.

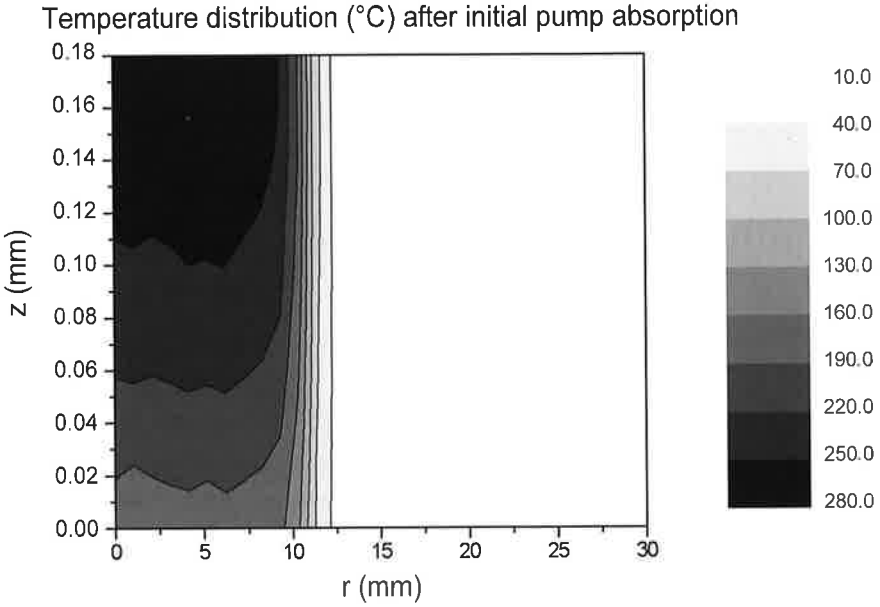

Fig. 5. Temperature after initial step of iteration (step 0): 9% Yb:YAG, thickness 180 μm, diameter 60 mm, 24 pump passes, pump spot diameter 22 mm, pump power 25.6 kW, soldered on 1 mm CuW, and cooling fluid temperature 15 °C.

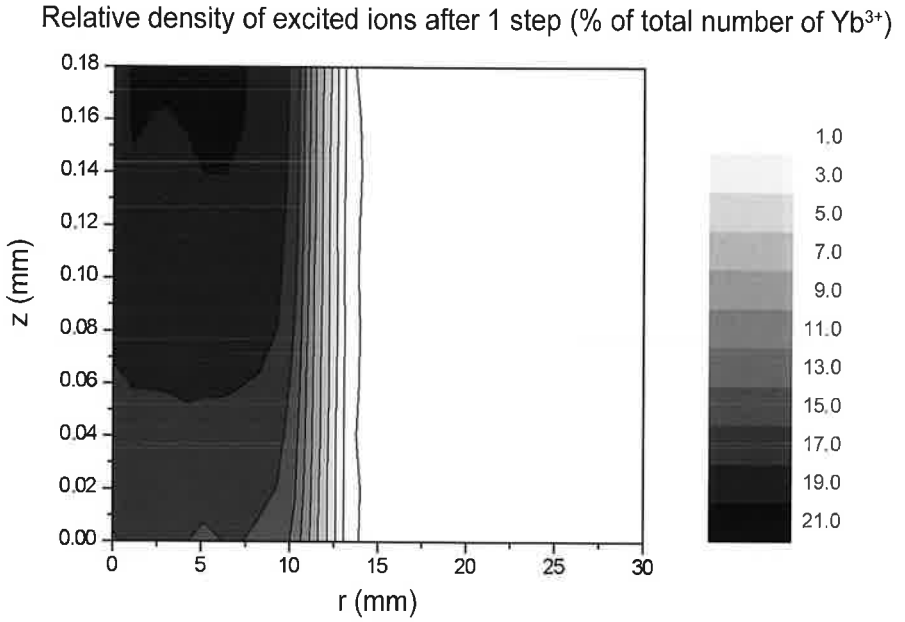

Fig. 6. Distribution of relative inversion density after step 1 of iteration: 9% Yb:YAG, thickness 180 μm, diameter 60 mm, 24 pump passes, pump spot diameter 22 mm, pump power 25.6 kW, soldered on 1 mm CuW, cooling fluid temperature 15 °C, and laser output power 17.95 kW.

The differential equation for the number of the excited ions can be solved in the quasi-steady state:

$$\tilde{N}_2 = \tau \cdot \frac{\dfrac{\lambda_p P_v}{2\pi\hbar c_{vac}} + \tilde{N}_0 \dfrac{\lambda_l M_r E_r}{2\pi\hbar c_{vac}} \sigma_{em,laser} f_{abs}}{1 + \dfrac{\lambda_l M_r E_r}{2\pi\hbar c_{vac}} \sigma_{em,laser} (1 + f_{abs})} \tag{19}$$

with the constraint

$$\ln(1 - L_{int}) + \ln(1 - T_{oc}) = -M_r \sigma_{em,laser} \int N_2 (1 + f_{abs}) - N_0 f_{abs}\, dz \tag{20}$$

derived from the resonator dynamics (transmission of output mirror T_{oc}, internal loss L_{int}).

Initial values for $\tilde{N}_2$ and E_r are derived analytically (with averaged crystal temperature and absorbed pump power density) and in an iterative procedure the laser power density and the number of excited ions are calculated, using

$$E_r^{(i)} = E_r^{(i-1)} \cdot \left[(1 - L_{int}) \cdot (1 - T_{oc}) \cdot \exp\left(M_r \sum_z \tilde{N}_2 (\sigma_{abs,l} + \sigma_{em,l}) - \tilde{N}_0 \sigma_{abs,l} \right) \right] \tag{21}$$

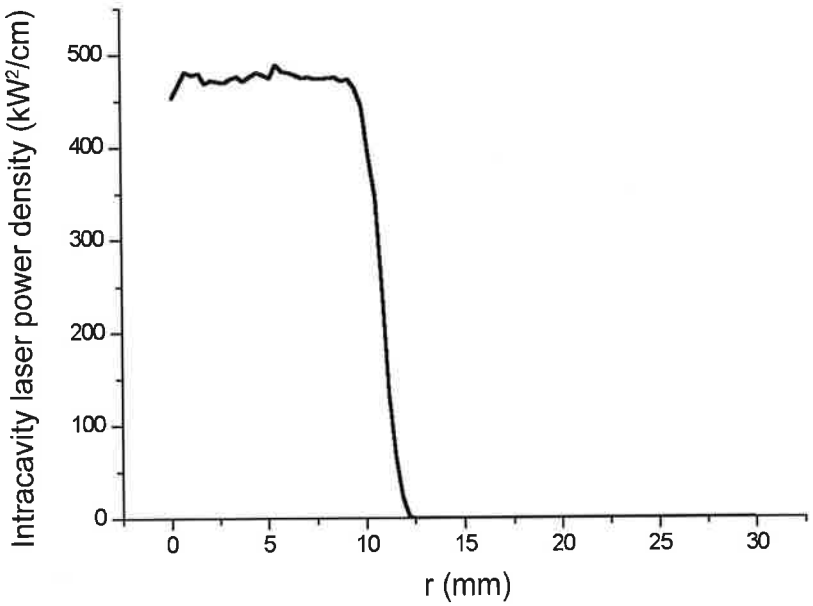

Fig. 7. Distribution of intracavity laser power density after step 1 of iteration: 9% Yb:YAG, thickness 180 μm, diameter 60 mm, 24 pump passes, pump spot diameter 22 mm, pump power 25.6 kW, soldered on 1 mm CuW, cooling fluid temperature 15 °C, and laser output power 17.95 kW.

to calculate a new $E_r^{(i)}$ from the previous $E_r^{(i-1)}$. With this new $E_r^{(i)}$, $\tilde{N}_2$ is modified according to Eq. (19). This procedure is repeated until the change of E_r is smaller than a given limit (typically 10^{-6}). From this resonator internal power density, the output power can be easily derived. Fig. 6 shows the inversion distribution after the first step is finished for the sample configuration, and Fig. 7 shows the radial distribution of the laser power density inside the cavity at the location of the disk.

As mentioned, the thermal behavior of the disk might also be influenced by the absorption of fluorescence radiation. Besides this influence on thermal properties, one can also expect the inversion density to be influenced by amplification of fluorescence. One possible method of calculation is based on Monte-Carlo ray tracing of fluorescence photons, described below.

A set of photons (number of photons N_{fluo}, typically 500,000) with a statistical distribution of wavelength (according to the emission spectra), starting coordinates (according to the density of excited ions), and propagation vectors are traced through the crystal. Absorption and amplification are computed for each volume element of the discretization. At the crystal boundaries, reflection and transmission are calculated either according to Fresnel formulas or based on angular reflection spectra calculated for dielectric coatings.

Each starting photon is traced separately; absorption, amplification, or transmission are represented by increasing or decreasing an integer value n_{fluo} associated with this starting photon and the photon is traced until n_{fluo} is zero.

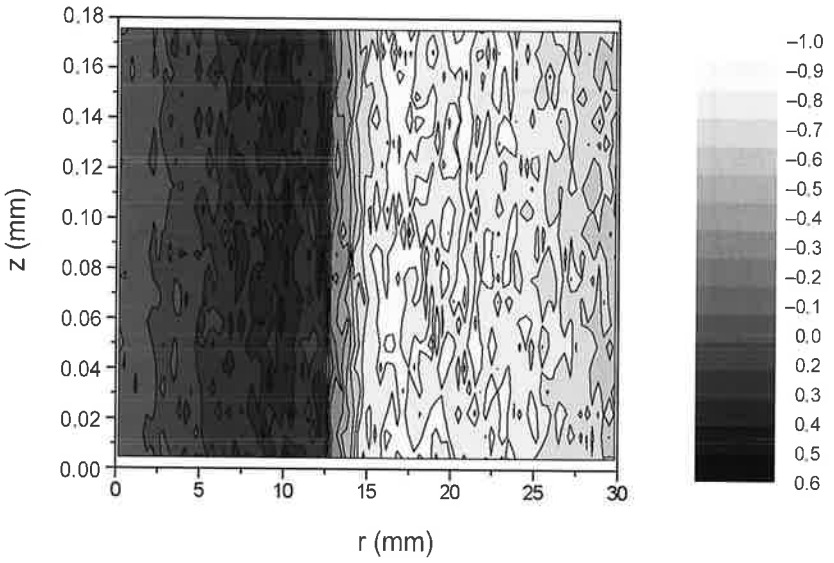

Fig. 8. Distribution of emission (>0) and absorption (<0) of ASE in relative units. Positive values are reduction of the inversion: 9% Yb:YAG, thickness 180 μm, diameter 60 mm, 24 pump passes, pump spot diameter 22 mm, pump power 25.6 kW, soldered on 1 mm CuW, and cooling fluid temperature 15 °C.

The change of n_{fluo} in each volume element is summed up for all starting photons, resulting in each element in a net change Δn_{fluo}. This can be scaled to a change of inversion ΔN_{ASE} in the volume element by

$$\Delta N_{ASE} = \frac{\Delta n_{fluo}}{N_{fluo}} \sum_{disk} \frac{\tilde{N}_2}{\tau} \tag{22}$$

This influence can be represented by a modified differential equation for the number of excited ions $\tilde{N}_2$ in each volume element,

$$\frac{\partial \tilde{N}_2}{\partial t} = \frac{\lambda_p P_V}{2\pi\hbar c_{vac}} + \frac{\lambda_l M_r E_r}{2\pi\hbar c_{vac}} \left(\tilde{N}_0 \sigma_{abs,l} - \tilde{N}_2 \left(\sigma_{abs,l} + \sigma_{em,l} \right) \right) - \frac{\tilde{N}_2}{\sigma} - \Delta N_{ASE} \tag{23}$$

The solution, Eq. (19), for N_2 in the quasi-steady state is now

$$\tilde{N}_2 = \tau \cdot \frac{\frac{\lambda_p P_V}{2\pi\hbar c_{vac}} + \tilde{N}_0 \frac{\lambda_l M_r E_r}{2\pi\hbar c_{vac}} \sigma_{em,laser} f_{abs} - \Delta N_{ASE}}{1 + \frac{\lambda_l M_r E_r}{2\pi\hbar c_{vac}} \sigma_{em,laser} \left(1 + f_{abs}\right)} \tag{24}$$

With this modified equation for $\tilde{N}_2$, the above-described step of calculating the laser power density and the number of excited ions is repeated.

Figure 8 shows the distribution of relative values of ΔN_{ASE} for the sample configuration; negative values are sources for the inversion. After this calculation of the excitation

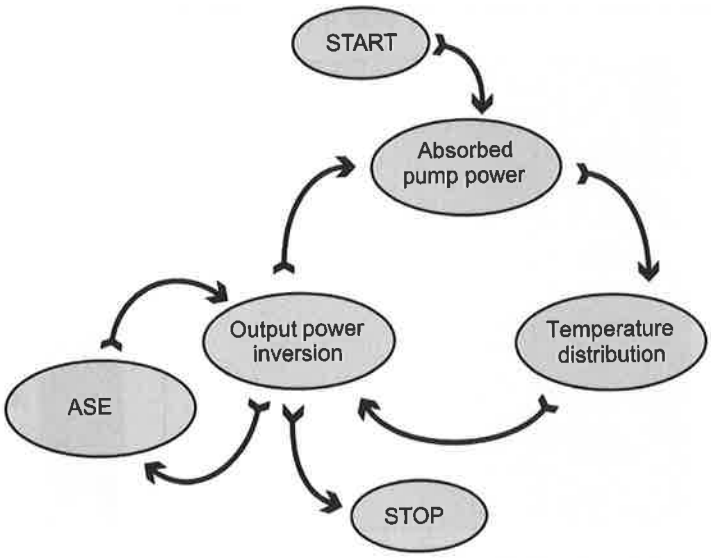

Fig. 9. Flow chart of the coupled modeling of absorption, temperature, and laser amplification, including ASE.

densities, the entire step, starting with the calculation of the absorbed pump power density, is repeated, but now with the changed N_2 distribution and temperature distribution. This large iteration is repeated until the change of laser output power and absorbed pump power is smaller than a given limit (typically 10^{e-4}). The sample configuration reaches this limit after four iterations. Fig. 9 shows the flow chart of this modified iteration scheme.

During this calculation, the absorption is typically reduced due to bleaching and temperature in the crystal. Consequently, heat generation and inversion density are also reduced. The ASE process results in redistribution of the inversion, especially in transfer of inversion to the unpumped region (Fig. 10). As a result of both effects, the possible output power is reduced; in the case of the sample configuration, the reduction is from 17.95 kW to 14.35 kW. The maximum crystal temperature is reduced from 280 °C to 260 °C. In Fig. 11, the initial and final values of the absorbed pump power density and the intracavity laser power density are compared. With the same configuration as for this sample but with different pump power values, the results in Fig. 12 are produced.

With this ray tracing of fluorescence photons, the power density transmitted through the HR-coated face of the disk can also be calculated. For a disk mounted on a heat sink, this power density is considered to be an additional heat source in the solder or glue layer and is included in the above-described temperature calculations.

4. Thermomechanical Modeling of the Thin Disk

As mentioned previously, an important question related to the thermal modeling of the thin disk is stress and deformation behavior. We can expect the mechanical properties of the heat sink or heat spreader to exert a strong influence. FEM modeling is a suitable calculation

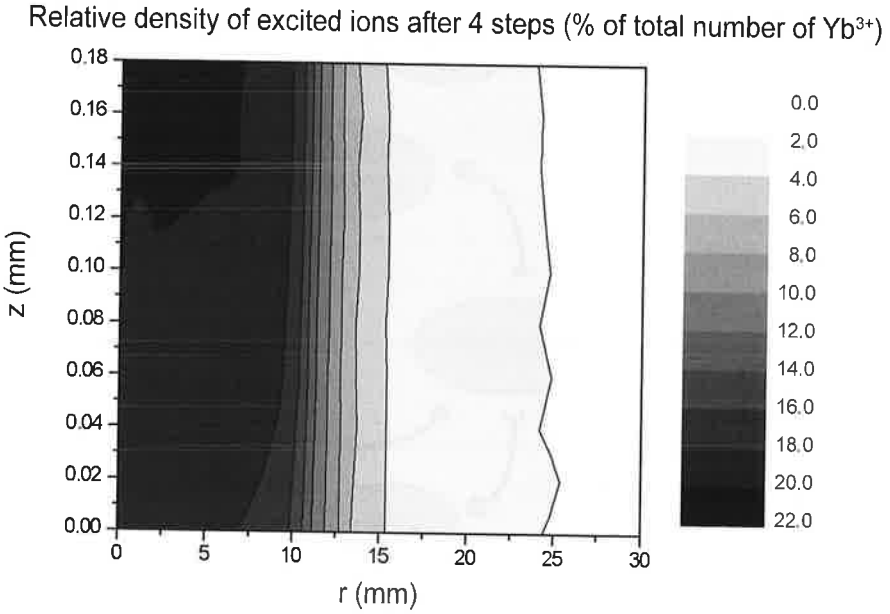

Fig. 10. Distribution of relative inversion density after final step of iteration: 9% Yb:YAG, thickness 180 μm, diameter 60 mm, 24 pump passes, pump spot diameter 22 mm, pump power 25.6 kW, soldered on 1 mm CuW, cooling fluid temperature 15 °C, and laser output power 14.35 kW.

method; steady-state heat conduction and steady-state strain-stress analysis are possible with several commercial FEM software packages. For the calculations presented in this paper, ABAQUS and Comsol Multiphysics were used. Due to the rotational symmetry of the problem (at least for rotationally symmetric heat loads), performing the calculations in reduced dimensionality is sufficient.

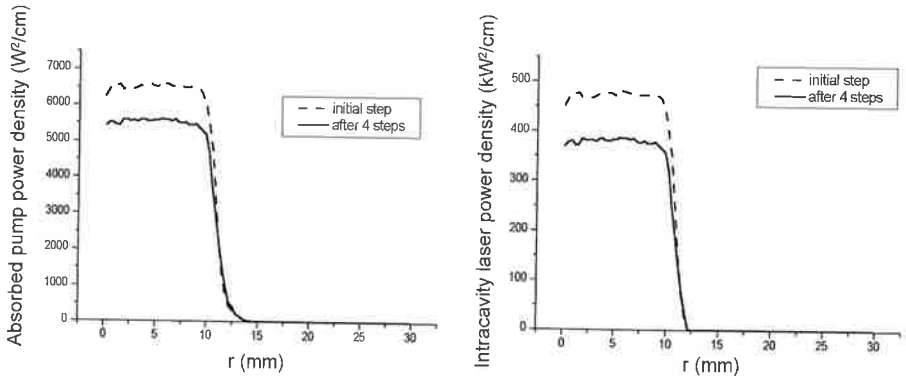

Fig. 11. Radial distribution of absorbed pump power density (*left*) and intracavity laser power density (*right*), comparison of initial and final values: 9% Yb:YAG, thickness 180 μm, diameter 60 mm, 24 pump passes, pump spot diameter 22 mm, pump power 25.6 kW, soldered on 1 mm CuW, and cooling fluid temperature 15 °C.

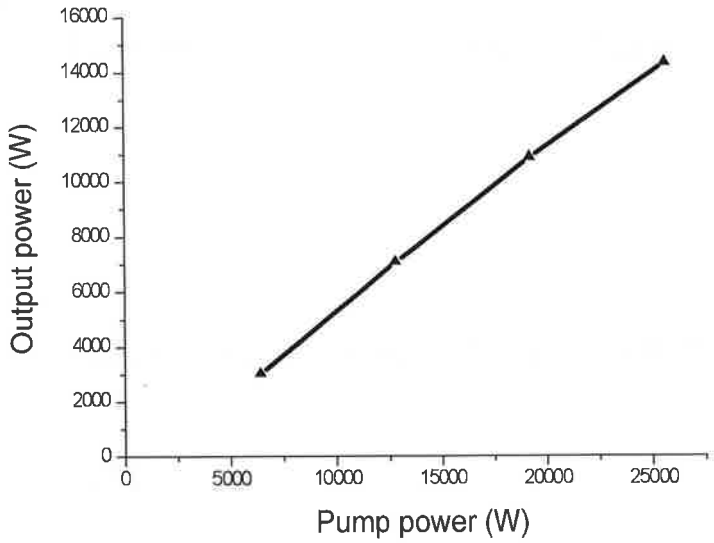

Fig. 12. Laser output power for cw operation: 9% Yb:YAG, thickness 180 μm, diameter 60 mm, 24 pump passes, pump spot diameter 22 mm, soldered on 1 mm CuW, and cooling fluid temperature 15 °C.

For the FEM analysis of thermomechanical behavior, heat source distribution calculated with the iterative model described in Section 3 can be used. Selected fundamental properties will be illustrated based on the sample configuration (see Table 1 and Fig. 12). The thermomechanical analysis is performed for three different mounting/cooling designs, depicted in Fig. 13:

- The "classical" design of a thin disk soldered on a heat sink
- A composite disk design, consisting of a thin Yb-doped disk and a 1-mm thick, undoped head-spreader cap, soldered on a heat sink (a very successful design for power scaling of microchip lasers and semiconductor thin disk lasers, seen in Kemp et al.[14])
- The same composite disk, but directly cooled

4.1. Temperature

In Fig. 14, the calculated temperature distribution for the three mounting designs is depicted. The pump power is 25 kW (pump power density = 6.5 kW/cm^2). The power and pump power density level are intended to be used for extremely high output power. For the classical design, the temperature in the homogeneous pumped center of the disk reaches 280 °C at the disk surface, whereas the temperature in the not-pumped region reaches only 20 °C (cooling fluid temperature 15 °C). The main temperature drop occurs at the edge of the pump spot over a width of only 2 mm. It is also remarkable that the temperature at the back side of the crystal is about 180 °C due to the temperature gradient in the coating, solder, and mount (CuW).

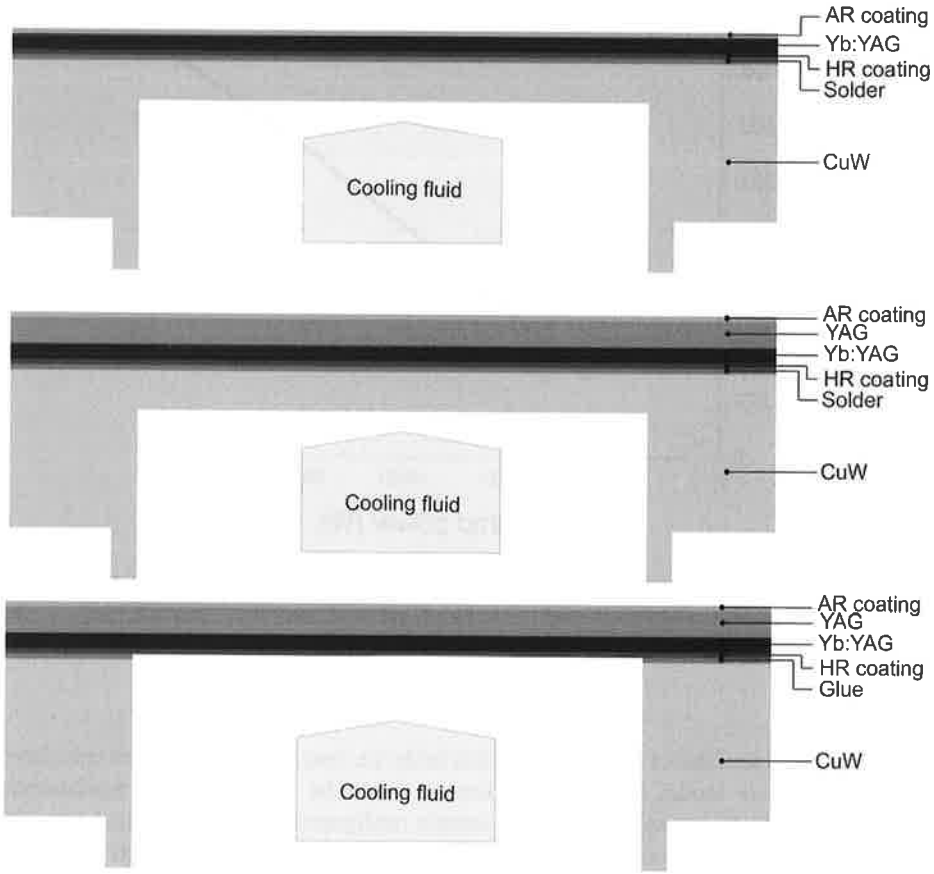

Fig. 13. Mounting designs. Top: Yb:YAG soldered on CuW ("classical" thin disk design). Middle: composite disk (Yb:YAG/YAG) soldered on CuW. Bottom: composite disk, directly cooled.

In the case of the composite disk on a heat sink, the undoped cap has nearly the same temperature as the upper surface of the doped region. Therefore, the maximum temperature is again 280 °C, but now for the complete thickness of the not-doped region. The radial temperature decrease is not as steep as for the classical design (4 mm). For such large pump spots, no significant temperature reduction by additional heat spreaders can be expected.

The most significant temperature reduction can be achieved with the directly cooled composite disk. The maximum temperature is reduced by about 120 °C, since there is no CuW and no solder between the disk and the cooling fluid. The width of the radial temperature-decrease region is 4 mm (similar to the soldered composite disk), and the temperature outside the pump spot is even closer to the temperature of the cooling fluid. In this case, the undoped cap also does not act as a heat spreader but it is necessary to increase the mechanical strength and enable the direct cooling without a supporting heat sink.

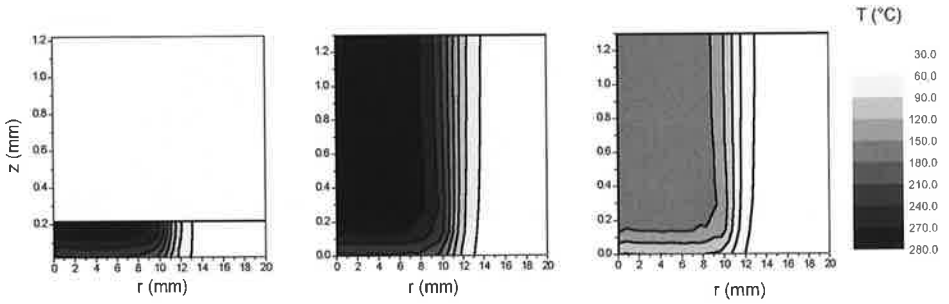

Fig. 14. Temperature distribution inside a soldered disk, pump power 25 kW, laser output power 14 kW, cooling from the bottom. Left: 200-μm disk soldered to CuW. Middle: bonded disk (Yb:YAG bonded to undoped YAG) soldered to CuW. Right: bonded disk (Yb:YAG bonded to undoped YAG) directly cooled.

4.2. Stress

Due to rotational symmetry, looking at the radial and azimuthal component of the stress tensor is sufficient; the stress components vertical to the plane of the disk are negligible. Fig. 15 shows stress distribution in the radial direction. For the soldered designs, only compressive stress can be found in this direction. The reason for this behavior is the expansion of the material in the radial direction with increasing temperature. In addition, there is some compressive pre-stress caused by the soldering process (the heat sink material has a thermal expansion slightly larger than YAG). The maximum compressive stress is nearly 600 MPa, but even this high stress is no problem for the disk and the laser operation.

The compressive radial stress is reduced for the directly cooled design due to the reduced temperature differences. Due to a small amount of radial heat flux in the undoped material, the heat expansion is smaller in the upper part. This causes bending of the disk, leading to a small amount of tensile radial stress at the bottom. In addition, as there is no heat sink, there is also no compressive pre-stress.

Figure 16 shows the azimuthal stress distribution, which displays some interesting features. For the soldered designs, only compressive stress exists with the same order of magnitude as the radial stress inside the pump spot. But outside the pump spot in the not-pumped region, we find high azimuthal tensile stress. The reason for this behavior is that not-pumped material is pressed by the radial stress inside the pump spot toward the outer edge of the crystal. This material then suffers from tensile stress.

The directly cooled design shows similar behavior, but as for the radial stress component, there is also some tensile stress in the pumped region due to bending. The benefits of the improved cooling are partially voided by the reduced stiffness of the design.

4.3. Design summary

In the case of a mounting design that ensures a stable and fixed mechanical contact of the disk to a stiff heat sink, there are two critical sources of stress inside the disk. First, if the difference of thermal expansion of the heat sink material and the laser material are too large,

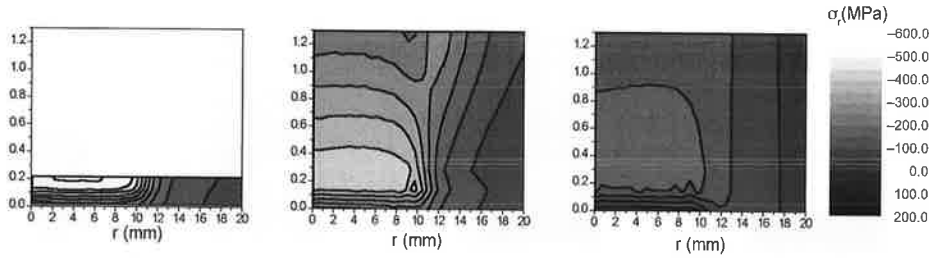

Fig. 15. Distribution of the radial stress inside a soldered disk, pump power 24 kW, laser output power 14 kW, cooling from the bottom via heat sink. Left: 200-μm disk soldered to CuW. Middle: composite disk (Yb:YAG bonded to undoped YAG) soldered to CuW. Right: composite disk (Yb:YAG bonded to undoped YAG) directly cooled.

this can cause radial stress during operation or during the mounting process. Especially when soldering the disk, a heat sink material with a thermal expansion much larger than the laser material will cause compressive stress during cooling down after soldering, leading to strong deformation of the disk. If the thermal expansion of the heat sink is too small, the soldering process will cause tensile stress inside the disk, causing rupture of the disk. Second, the disk will heat up during operation in the pumped region; the unpumped region will be colder. This causes strong azimuthal tensile stress in the cooler region around the hot pumped part of the disk. This tensile stress increases with pumped region volume and pump power density. It can be partially compensated by pre-stress, which is caused by the soldering process using a heat sink material with a thermal expansion slightly larger than the laser material.

In the literature, a large variation of values of tensile strength of YAG can be found, as the tensile strength of crystalline materials like YAG partly depends on surface quality. In Marion,[15] this influence was studied, and for polished YAG, a tensile strength of 175 MPa was measured. Based on this value and including a safety factor of 15%, a tensile stress of more than 150 MPa is considered critical tensile stress.

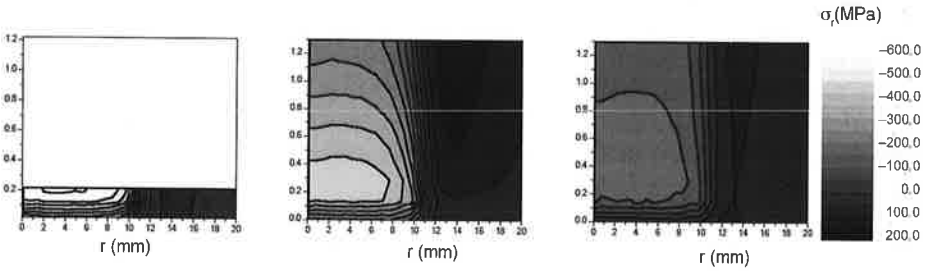

Fig. 16. Distribution of the azimuthal stress inside a disk, pump power 25 kW, laser output power 14 kW, cooling from the bottom via heat sink. Left: 200-μm disk soldered to CuW. Middle: composite disk (Yb:YAG bonded to undoped YAG) soldered to CuW. Right: composite disk (Yb:YAG bonded to undoped YAG) directly cooled.

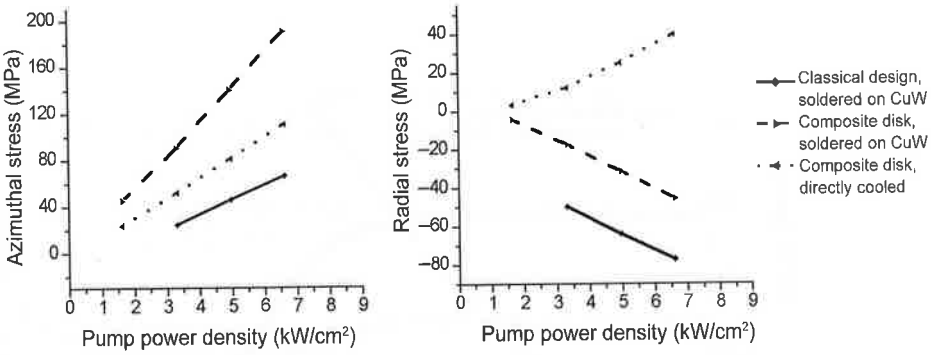

Fig. 17. Comparison of the maximal radial and azimuthal stress inside the disk for the three mounting designs.

Figure 17 summarizes the results for all three designs, showing the maximum radial and azimuthal stress as functions of pump power density for a pump spot diameter of 22 mm. For the "soldering design" and the "modified soldering design," the radial stress behavior is dominated by the CuW heat sink. The heat sink limits expansion and bending of the thin disk. This leads to compressive stresses in the thin disk. For the "direct cooling design," the radial stress behavior is different, as the thin disk can bend to follow varying heat expansions. This leads to tensile stress at the bottom of the thin disk. Due to the lower temperatures in the "direct cooling design," this tensile stress does not reach critical values.

The "classical" design shows the smallest azimuthal stress values due to stress compensation by the heat sink. With the soldered composite disk, the amount of hot material is too large to be compensated by the heat sink, so the maximal pump power density is limited to values of about 5 kW/cm². As the temperatures are much lower for the directly cooled design, it can be used despite the fact that there is no stress compensation via CuW.

The directly cooled design offers several benefits for high power laser operation with high efficiency and good beam quality. In addition, this design shows high reduction of ASE effects, which may cause a lot of problems for other designs.[16] One drawback is that larger distortion at the edge of the pump spot compared to the classical design can be expected as there is more hot (undoped) material inside the resonator.

5. Thermal Lens

From the data calculated with the FEM model, the thermal lens of the thin disk can also be calculated. From the distribution of temperature and strain and the deformation of whole system including heat sink/heat spreader, the optical phase distortion (OPD), $\Phi(r)$, is calculated as follows:

$$\Phi(r) = 2\frac{2\pi}{\lambda_l}\left[\int_0^{d_{Kr}}\left[n_0 + \frac{\partial n}{\partial T}\left(T(r,z) - T_0\right) - 1\right]\cdot\left[1 + \varepsilon_z(r,z)\right]dz - z_0(r)\right] \qquad (25)$$

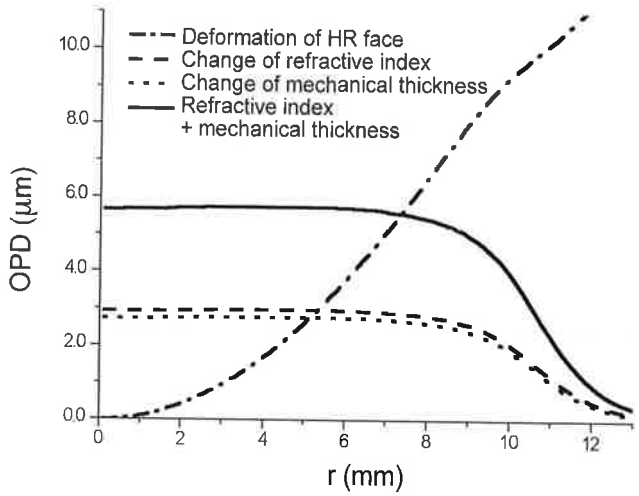

Fig. 18. Calculated phase deformation OPD for directly cooled thin disk, pump diameter 22 mm, pump power 25 kW. The figure shows the various fractions of the OPD.

with n_0 the refractive index at T_0, $\frac{\partial n}{\partial T}$ the thermo-optical coefficient, ε_z the strain in the z-direction, and z_0 the displacement of the HR side of the disk.

First, we expect a defocusing influence resulting from the axial temperature gradient, which causes a bending of the complete system (disk and support). The dash-dot line in Fig. 18 shows this contribution to the OPD. Opposite this defocusing part are two focusing contributions resulting from the thermal expansion and the change of the index of refraction with increasing temperature. Both contributions are proportional to the temperature distribution; they are shown in the figure as dotted and dashed lines. The sum of both, shown as a solid line, would be the equivalent to what is usually calculated as thermal lens, such as for rod lasers. The resulting OPD is mainly defocusing with a phase step at the edge of the pump spot.

Figure 19 shows the OPD as the sum of the above-described contributions for the three discussed mounting designs; it can be seen that the total OPD is strongly reduced for the "direct cooled design" compared to the other two designs. This is due to two effects: (1) the temperatures in the "direct cooled design" are significantly reduced; and (2) there is no heat sink in the "direct cooled design," and the temperature gradient in this heat sink is the source of the largest contribution to the OPD in the other designs.

To analyze the influence of the phase distortion more quantitatively, the OPD must be separated in a spherical and an aspherical part. Starting with a Gaussian fundamental mode,

$$\mathrm{E}(r) = \sqrt{\frac{2}{\partial w^2}} \exp\left(-\frac{r^2}{w^2} + i\phi\right) \tag{26}$$

and a phase distortion of the disk,

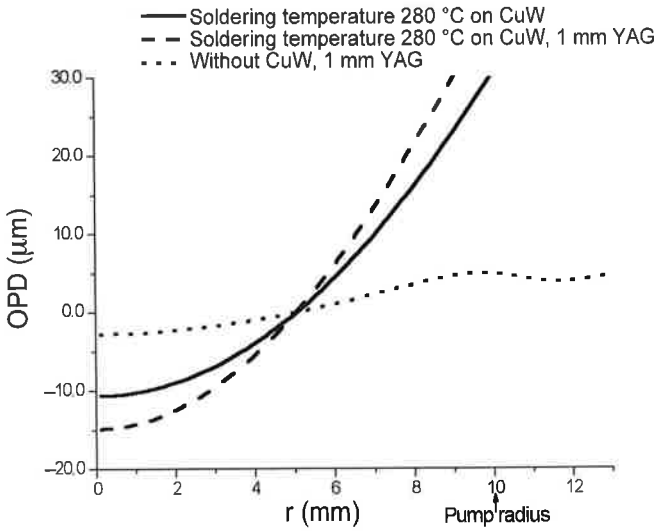

Fig. 19. Calculated total OPD of a classical soldered disk, a soldered composite disk bonded (Yb:YAG bonded to YAG) and a directly liquid cooled disk (pump diameter 22 mm, pump power 25 kW).

$$\Phi(r) = -\frac{2\pi}{\lambda}\frac{r^2}{R_L} + \Delta\Phi(r) \tag{27}$$

one gets the following after one pass through the disk:

$$\tilde{E}(r) = \sqrt{\frac{2}{\partial w^2}}\exp\left(-\frac{r^2}{w^2} + i\varphi - i\frac{2\partial}{\lambda}\frac{r^2}{R_L} + i\Delta\Phi(r)\right) \tag{28}$$

Projection on a suitable set of Gauss-Laguerre-Modes gives

$$c_{00} = \iint \tilde{E}E_{00}^{*} r\,dr\,d\psi = 2\pi\int\sqrt{\frac{2}{\pi w^2}}\exp\left(i\Delta\Phi(r)\right)\exp\left(\frac{-2r^2}{w^2}\right)r\,dr \tag{29}$$

Defining $L_B = 1 - |c_{00}|^2$ as fundamental mode diffraction loss, $\langle f(r)\rangle = \frac{4}{w^2}\int f(r)e^{-2\frac{r^2}{w^2}}rdr$ and using an approximation for c_{00} (neglecting terms of more than quadratic order in $\Delta\Phi$), it is possible to write

$$L_B \approx \left\langle \Delta\Phi(r)^2 \right\rangle - \left\langle \Delta\Phi(r)\right\rangle^2 \tag{30}$$

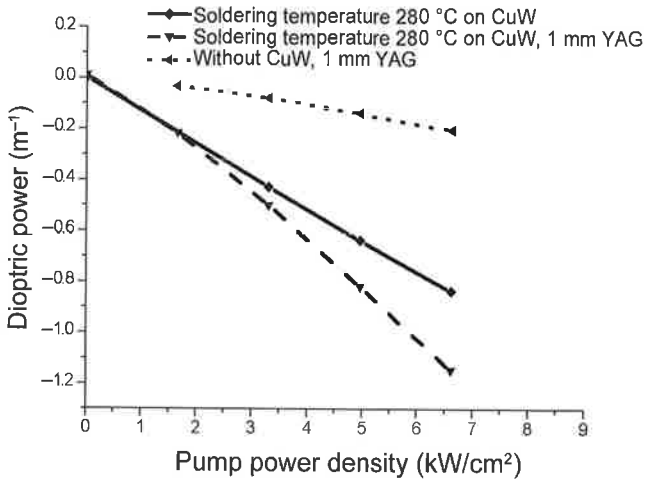

Fig. 20. Calculated spherical portion of the thermal lens of a soldered disk, a bonded disk (Yb:YAG on undoped YAG) and a directly liquid cooled disk (pump diameter 22 mm, pump power 25 kW).

It can be shown that L_B is minimized if

$$\frac{1}{R_L} = \frac{\lambda}{2\pi} \frac{\left\langle \Delta\Phi(r) r^2 \right\rangle - \left\langle \Delta\Phi(r) \right\rangle \left\langle r^2 \right\rangle}{\left\langle r^2 \right\rangle^2 - \left\langle r^4 \right\rangle} \tag{31}$$

These expressions can be easily evaluated, giving the focal length $f_L = \frac{R_L}{2}$ or the dioptric power of the OPD and the remaining aspherical phase distortion.

Figure 20 shows the optical power as a function of the pump power density for a pump spot diameter of 22 mm for the three discussed mounting designs at different pump power densities. The optical power is about 0.1 m^{-1} per kW/cm^2 pump power density for the classical design and even more for the soldered composite disk. As the deformation of the heat sink is the main contribution to the spherical part, the dioptric power is minimized in the "direct cooled design."

If we compare the remaining aspherical parts of the OPD for all three designs (Fig. 21), then we see that all the designs look very similar inside the pump spot. But the range of the phase without distortion is much wider for the classical design than for the others. The reason is that for the other designs, the temperature decrease starts much earlier and is much broader than for the soldering design.

6. Calculations Concerning Pulsed Operation

Since the lifetime of the excited state of Yb:YAG is about 1 ms, this material should be capable of storing very high energies (e.g., 10 J with a system that is capable of delivering

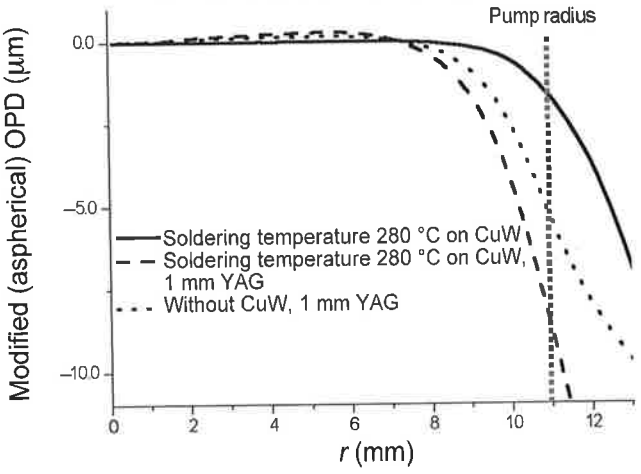

Fig. 21. Calculated aspherical portion of the OPD of a soldered disk, a soldered composite disk (Yb:YAG on undoped YAG), and a directly liquid cooled disk (pump diameter 22 mm, pump power 25 kW).

10 kW in cw operation); several hundreds of millijoules are reported in the literature (including in Stolzenburg et al.[17]). This consideration is correct in principle, but one must recall that at low repetition rates the gain inside the disk is about 10 times higher than during the saturated cw operation. This leads to a strong reduction of the stored energy (of the density of the excited ions) by ASE; moreover, the small signal gain is reduced. Several attempts were made in recent years to study this effect and to find scaling limits (e.g., Contag et al.,[3] Contag,[4] Kouznetsov et al. (2006)[18] and (2008)[16]). The models show that the demonstrated output powers are far below the scaling limits due to ASE. They also show that ASE effects limit the possible pulse energy to values of a few joules, using the typical high-power, cw, thin-disk laser design. Designs optimized for pulse amplification can also reach higher pulse energies, especially if they are quasi-cw pumped with a moderate duty cycle.

6.1. Results with the quasi-static model

The model presented in Section 3 can also be used to describe a thin disk that is pumped without a resonator (the output power is no longer a suitable criterion for convergence, but one can, for example, perform a limited number of iterations and manually check whether parameters like gain and absorbed pump power converge). From the calculated density distribution of excited ions, the small signal gain and the extractable energy can be easily derived.

Figure 22 shows numerical results for a soldered thin disk. It can be seen very clearly that the gain increases with increasing pump power density, but with a bigger pump spot diameter the gain is much smaller than for the smaller pump spot diameter. To study this effect in more detail, Fig. 23 shows the stored energy inside such a disk with constant

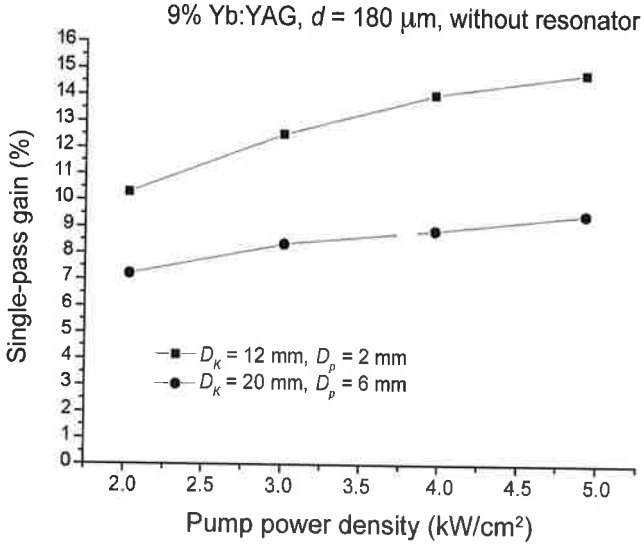

Fig. 22. Calculated small signal gain of a disk as function of the pump power density for different pump diameters; disk soldered onto CuW.

absorbed pump power density (value 3 kW/cm²) but with a varying pump spot diameter. The effect of the gain reduction with increasing pump spot diameter leads—after a quadratic increase of the energy—to a more linear increase of the stored energy. For even larger pump spot diameters, the stored energy is further reduced.

The quasi-static model is principally suitable to analyze the influence ASE on the performance of a thin disk laser. The treatment of ASE with Monte-Carlo ray tracing is very flexible and can also handle spatial variations of gain or temperature. Even spatial variations of thin disk face reflectivity could be handled.

The iterative quasi-static approach represented by Eq. (24), however, limits the validity of the model to situations where the influence of the ASE is a "small" perturbation. Following Barnes and Walsh,[19] ASE influence can be approximated by $\Delta N_{ASE} \sim N_2^2$; therefore, the assumption of a small perturbation is not suitable in situations with a high density of excited ions in large-volume and high transversal gain, such as thin disk lasers for high energy pulse extraction. The convergence problems of the quasi-steady state iterative model are described in Contag,[4] limiting predictable output power in cw operation to roughly 50 kW and the predictable energy to 2.5 J. In the next section, a time-resolved approach for this situation will be discussed.

6.2. Time-resolved model

To evaluate designs for higher pulse energies in greater detail, a time-resolved numerical model of pump absorption and ASE can be used. This model must account for the spectral distribution of the spontaneous emission, the spectral and spatial distribution of emission and absorption, and the spectral and angular transmission of surfaces or coatings. Interesting

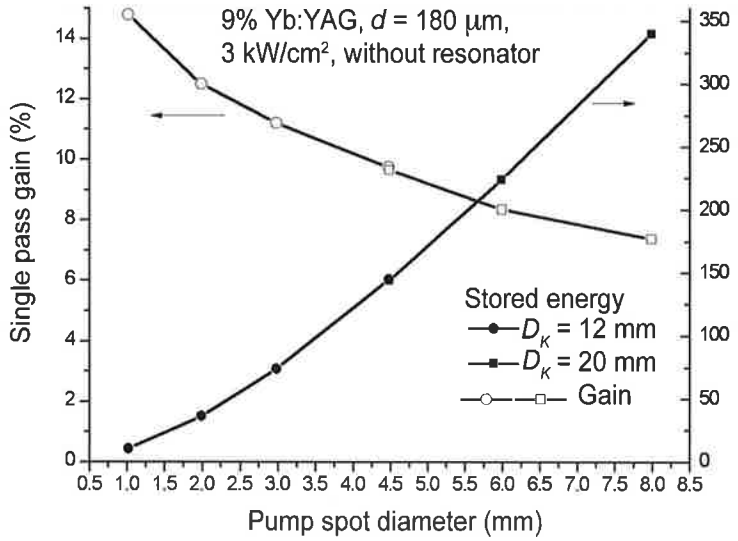

Fig. 23. Calculated stored energy and single-pass small signal gain in one disk as function of pump diameter; disk soldered onto CuW.

approaches for calculating the ASE influence on lasers with a large aperture-to-length ratio were made in the past for KrF lasers (see, for instance, Lowenthal and Eggleston,[20] Okuda and Shaw,[21] and Sasaki et al.[22]). These models can be partially applied to thin disk lasers; the model is also discussed in Speiser and Giesen[23] and Speiser.[24]

Interaction of ASE and excitation

The fundamental equation of motion (Eq. (1)) for the density of excited ions N_2 in a pumped active medium without resonator, including ASE but no additional effects such as upconversion, is

$$\dot{N}_2 = Q - \frac{N_2}{\tau} - \iint \gamma_\lambda \Phi_{\lambda,\Omega} d\lambda d\Omega \tag{32}$$

with Q the source (e.g., the absorbed pump photons per volume and time) and τ the fluorescence lifetime, γ_λ the gain per length at the wavelength λ (gain coefficient), and $\Phi_{\lambda\Omega}$ the number of (amplified) fluorescence photons per area and time (photon flux density) coming from the solid angle Ω.

First, it is necessary to calculate the photon flux density. With excitation density $N_2(\vec{s})$ and gain coefficient $\gamma_\lambda(\vec{s})$, one gets at the point $\vec{s} = 0$ from a volume element dV at a distance $s = |\vec{s}|$ in the direction $\hat{s} = \vec{s} / s$ as follows:

$$d\Phi_{\lambda\Omega}(\vec{s}) = \beta_{\lambda\Omega} \frac{N_2(\vec{s})}{\tau} \frac{1}{4\pi s^2} g_\lambda(\vec{s}) dV \tag{33}$$

with β_λ the spectral distribution of the fluorescence, fulfilling $\int\beta_\lambda d\lambda = 1$ and

$$g_\lambda(\vec{s}) = \exp\left(\int_0^s \gamma_\lambda(\tilde{s}\hat{s})d\tilde{s}\right) \tag{34}$$

the amplification of the photon flux density.

The entire photon flux density at wavelength λ from the direction $\hat{s}$ can be calculated by

$$d\Phi_{\lambda\Omega}(\hat{s}) = d\Omega\frac{\beta_\lambda}{\tau}\int_0^{s_{\max}} N_2(\hat{s}s)g_\lambda(\hat{s}s)ds \tag{35}$$

using $dV = s^2 d\Omega$. The maximum integration distance $s_{\max}$ depends on the analyzed geometry. The thin disk is a cylindrical volume of height (thickness) h and radius R, the faces of the cylinder orientated horizontally (Fig. 24). No reflection from the lateral surface is taken into account; with reflections from the lateral surface, no maximum integration distance can be defined.

The reflectivity of the faces of the cylinder will be given by the functions $AR(\lambda,\partial)$ ("antireflective") and $HR(\lambda\partial)$ ("highly reflective"); the AR face is on the top and the HR face at the bottom. The AR face is typically the interface between the crystalline laser medium and air (or vacuum), and antireflective for normal incidence at the laser and pump wavelengths. For the model, it is assumed that it is nonreflective for angles smaller than the critical angle of total reflection $\partial_{tr} = \arcsin(1/n)$, with n the index of refraction of the active medium, and ideally reflecting for larger angles. The HR face will fulfill $HR(\lambda,\partial) \neq 0$ for all ∂ due to technical limitations of the coating design.

In spherical coordinates, Eq. (35) transforms to:

$$d\Phi_\lambda(\varphi,\theta) = \sin\theta d\theta d\varphi\frac{\beta_\lambda}{4\pi\tau}\int_0^{s_{\max}} N_2(s,\varphi,\theta)g_\lambda(s,\varphi,\theta)ds \tag{36}$$

Taking into account the multiple reflections at the faces of the cylinder, $s_{\max}$ can be expressed by

$$s_{\max} = \frac{\sqrt{R^2 - \rho\sin^2\varphi} - \rho\cos\varphi}{\sin\theta} \tag{37}$$

if $AB(\lambda,\partial)HR(\lambda,\partial) \neq 0$.

To account for losses at the AR and HR faces, the gain coefficient is modified to

$$\bar{\gamma}_{\lambda,\theta} = \gamma_\lambda + \frac{\ln(AR(\lambda,\theta)HR(\lambda,\theta))}{2h}\cos\theta \tag{38}$$

if $AB(\lambda,\partial)HR(\lambda,\partial) \neq 0$.

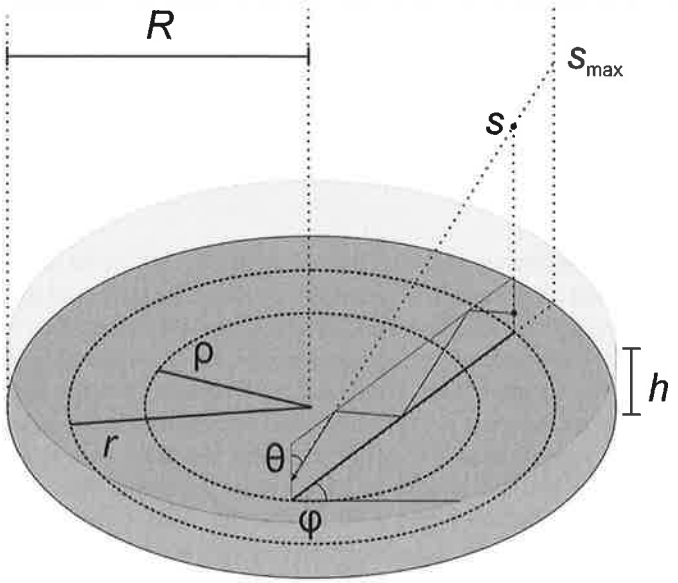

Fig. 24. Geometry of the thin disk.

Numerical model

Based on these considerations, it is possible to develop a numerical model of the interaction of amplified spontaneous emission and excitation. The problem is discretized in ρ, ∂, φ, and λ. Neglecting the variation of excitation and gain in the axial direction and assuming rotational symmetry, only the radial variation of $N_2(r)$ and $\lambda_2(r)$ remains.

The temporal development of the excitation can easily be calculated by integrating the differential Eq. (32) with implicit methods. For each time step, the source Q and the photon flux densities $d\Phi_\lambda(\hat{s})$ are calculated based on the distribution of excitation from the previous time step. As the typical time constant of the excitation is in the order of the spontaneous lifetime (several hundreds of microseconds), this is adequate for time steps of a few microseconds.

It would be possible to calculate the integrals in Eqs. (32) and (36) by transforming from integration in ds to integration in dr (i.e., in "radial" coordinates), but this will introduce integrals like

$$\int \frac{f(r)rdr}{\sin\theta\sqrt{r^2-\rho^2\sin^2\varphi}} \tag{39}$$

For analytical consideration, such as assuming a homogenous density of excitation and $f(r)$ constant, this can easily be handled. But the numerical calculation of such integrals with a simple trapezoidal rule is typically not converging. It is necessary to use some kind of Gaussian quadrature, interpolating $f(r)$ at appropriate nodes.

Alternatively, it is possible to choose for each radial position ρ_i and each angle φ_k a set of equidistant nodes $a_{i,k,l}$ on the trace between ρ_i and the lateral surface of the disk. With a linear interpolation of the gain coefficients $\gamma_\lambda(r_j)$ and the excitation density $N_2(r_j)$ on these nodes, a trapezoidal rule can be used for the integration on such a trace. This method was used to calculate the results presented in subsequent sections.

Scattering

As mentioned in the previous section, ideal transmission of the ASE at the lateral surface of the disk was assumed. This could be realized technically by absorbing layers and special structuring of this surface. But actual thin-disk laser designs do not use these possibilities. Typically, some amount of the ASE is reflected and some is just scattered due to surface roughness.

The simplest way to implement some kind of feedback from the lateral surface in the model is to add an isotropic source of fluorescence photons at the outermost node of the radial discretization. This source can be treated in the same way as the spontaneous emission at this node and can simply be added to it. By setting this source to a value equivalent to a certain fraction of the ASE photon flux density that reached the lateral surface in the previous time step, a model for an isotropic scattering of this fraction of the ASE at the surface is derived.

This approach has an important drawback. The scattered photon flux density is amplified and partially reaches again the lateral surface, and then is scattered again, amplified, and so on. This would be described correctly only by a model for an ASE photon number enclosed in the disk, having some sources, loss and absorption, and amplification. In addition, an artificial speed of light is introduced by using values of the previous time step, depending on radial position and step length. Therefore, the temporal evolution of the ASE photon flux density is not described correctly.

Nevertheless, the model can be used to explore the influence of the feedback, if the feedback is small and the amplification is not too high.

6.3. Results

In Speiser,[24] the model is used to analyze the optimization possibilities for a low-repetition-rate thin disk amplifier. The results taken from Speiser[24] show the potentials as well as limitations of the model.

Typical high-power thin disk design

The first analyzed design is a moderately doped Yb:YAG disk with a thickness of 150 μm and a diameter of 25 mm. A pump power of 4 kW on a pump spot diameter of 11.6 mm with 24 pump beam passes was applied. These are parameters that would be typical for cw or high repetition-rate operation. For low repetition-rate and high energy operation, it would be useful to reduce the duty cycle, so a pump pulse duration of 1 ms was used.

Figure 25 shows the achievable gain for different values of the fraction of ASE reaching the lateral surface of the disk and also for the situation without any ASE. The ASE strongly reduces the achievable gain and with the feedback from the lateral surface, the gain shows a rollover after about 300 μs.

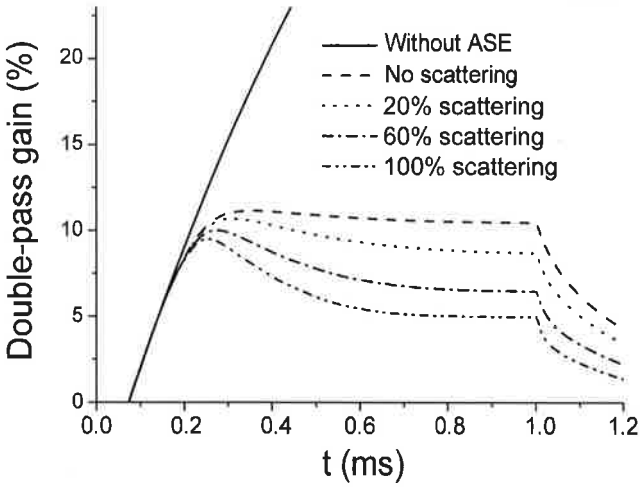

Fig. 25. Double-pass gain for different values of scattering: 12% Yb:YAG, thickness 150 μm, pump power 4 kW, pump pulse duration 1 ms, and pump spot diameter 11.6 mm.

Maximum extractable energy will be about 290 mJ with ASE (with some feedback, only 250 mJ and rapidly dropping after 300 μs) compared to more than 1 J without ASE. Obviously, this design is not optimized for high energy extraction.

Design for reduced duty cycle

As we assume a reduced duty cycle, we can increase pump power density and crystal thickness. The increased thickness and reduced pump spot diameter will reduce ASE influence. Fig. 26 shows the calculated extractable energy for a 600-μm thick thin disk and increased pump power density. Without scattering and with 60% scattering, no rollover occurs; it would be necessary to use a longer pump pulse duration to evoke it. The maximum extractable energy with 60% scattering is about 680 mJ, and without scattering about 760 mJ. Without ASE, we could reach an extractable energy of more than 1.6 J, but only with a much longer pulse duration and therefore higher thermal load.

Thermal load and efficiency are important design criteria, as well as the ratio of extractable to pump energy. Fig. 27 shows that maximum efficiency is reached for pump pulse durations significantly shorter than 1 ms, with and without ASE. The ASE moves the optimum toward shorter pump pulse durations; it can be expected that the optimum is shifted to shorter pump pulse durations for larger pump spots. This reduction of optimum pump pulse duration can be used to further reduce duty cycle and thermal load, and either increase the pump power density or the thickness of the disk.

Model limitations

As mentioned previously, the time-resolved model works quite well also for high transversal gain. But modeling the feedback is not really adequate for high transversal gain and high

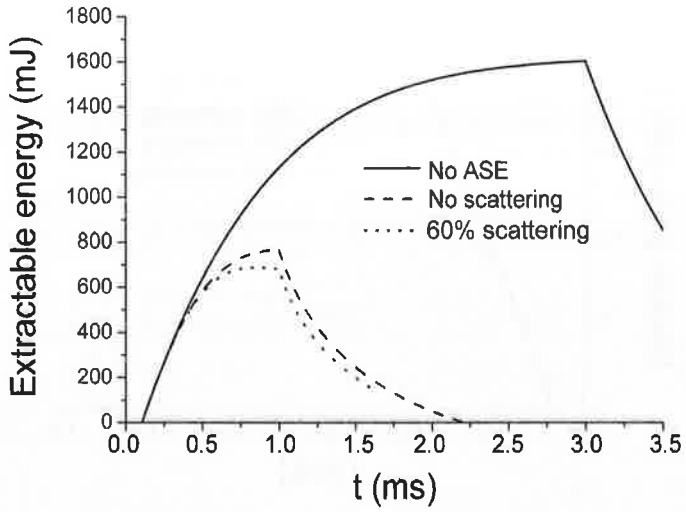

Fig. 26. Extractable energy for 4.5% Yb:YAG, thickness 600 μm, pump spot diameter 9.8 mm, and pump power 4 kW.

reflection or backscattering at the lateral surface. If we look at a simulated gain of a 300-μm thick thin disk, 9%Yb:YAG, pumped with 16 kW at a 12.4-mm pump spot diameter, we see not a rollover but something like a spike with backscattering of 60% (Fig. 28). For this configuration, the laterally emitted ASE power was calculated, which also shows also a spike.

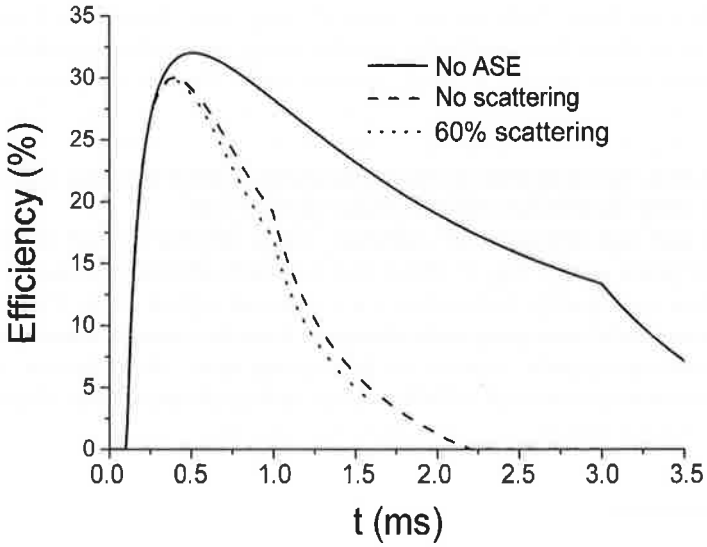

Fig. 27. Efficiency for 4.5% Yb:YAG, thickness 600 μm, pump spot diameter 9.8 mm, and pump power 4 kW.

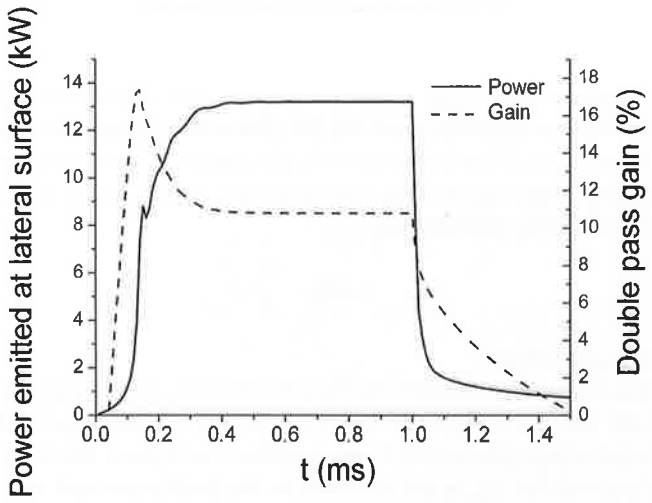

Fig. 28. Laterally emitted power and double pass gain: 9% Yb:YAG, thickness 300 μm, 16 kW pump power, and 12.4 mm pump spot diameter.

We can enhance this behavior if we reduce the concentration of active ions to 4.5%. In this case, the absorption in the unpumped area is strongly reduced. In Fig. 29, we can see the spike in the gain more clearly, and the laterally emitted power shows some kind of relaxation oscillations. Obviously, the relaxation oscillation frequency is determined by the ASE photon lifetime, and therefore it is strongly influenced by the abovementioned "artificial speed of light."

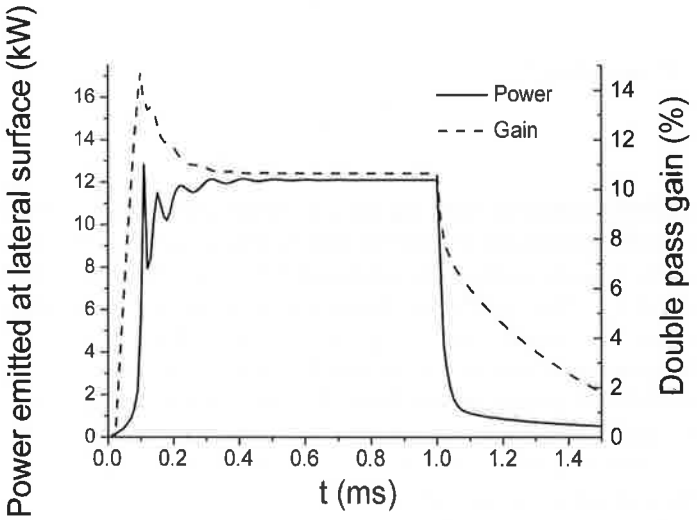

Fig. 29. Laterally emitted power and double pass gain: 4.5% Yb:YAG, thickness 300 μm, 16 kW pump power, and 12.4 mm pump spot diameter.

7. Ultimate Scaling Limits

After finding solutions for many design problems (cooling, thermally induced stress, etc.), the inversion depletion due to ASE inside the disk is the remaining limiting effect for the thin disk design. Various approximations for this influence as a base for estimating scaling limits can be found in the literature. In general, the influence of the ASE can be described as lifetime reduction of the excited state, expressed by reduced lifetime τ_{ASE}. In Kouznetsov et al.,[18] reduced lifetime is calculated as

$$\tau_{ASE} \sim \tau \exp\left(-\frac{2r_p}{h} g\right) \tag{40}$$

with r_p the pump spot radius.

Based on this expression, estimates for the maximum possible output power for a single disk are derived. The most important result is that the maximum possible power (and also the maximum achievable power if one specifies a minimum efficiency), scales with the inverse of internal loss L_{int} in the resonator to the third power and with the square of the maximum-allowed product of pump power density and thickness C_{th} ("thermal load parameter" or "thermal shock parameter"), that is,

$$P_{out,\max} \sim C_{th}^{\ 2} \cdot L_{int}^{\ -3} \tag{41}$$

Based on considerations similar to the ideas presented in the "Interaction of ASE and excitation" section and Fig. 24, in Speiser[25] a slightly different expression for the reduced lifetime was found:

$$\tau_{ASE} \approx \frac{\tau}{\exp(2g) + 2g\,\mathrm{Ei}\left(\frac{2gr_p}{h}\right) + 2g\,\mathrm{Ei}(2g)} \tag{42}$$

This can be approximated by

$$\tau_{ASE} \sim \tau \frac{r_p}{h} \exp\left(-\frac{2r_p}{h} g\right) \tag{43}$$

With the lifetime reduction from Eq. (42), a similar dependence of maximum output power from the internal loss and the thermal load parameter as in Kouznetsov et al.[18] can be derived. In Table 2, some results of the optimization for maximum output power are given for two values of L_{int}. These results are clearly beyond actual possible or planned thin disk designs, but more than 20 MW from a single disk seems feasible if L_{int} is reduced to 0.25%. However, the latter would require a pump spot diameter of ~5.5 m.

The achievable efficiencies are small (less than 10%), but following Kouznetsov et al.[18] and Speiser,[25] higher efficiencies are possible with a slightly different optimization. With L_{int} = 0.25%, 1 MW of laser power is possible with nearly 50% optical–optical efficiency, requiring only a 20-cm pump spot diameter.

With the same considerations, the maximum extractable energy can also be calculated; Table 3 provides selected results of this optimization. For a pulsed system that typically

Table 2. Maximum achievable output power and optimized design parameters for different values of resonator internal loss

Internal losses L_{int}	1%	2%
Reduced lifetime τ_{ASE}	483 μs	412 μs
Optimized doping concentration N_0	0.93%	1.51%
Thickness h	0.87 mm	0.56 mm
Pump radius r_p	363 mm	109 mm
Pump power P_{pump}	5.9 MW	830 kW
Output power P_{out}	574 kW	75 kW

Data values from Speiser, J., J. Opt. Soc. Am. B **26**(1), 26 (2009).

contains polarizers and electro-optical switches, an internal loss of L_{int} = 4% is close to realized systems, and a pulse energy of 8.3 J is also close to realized thin disk pulse lasers.

For all these calculations, the thermal load parameter was set to C = 10 W/mm (equivalent to 5 kW/cm² pump power density on a 200-μm thin disk), creating a temperature difference of 75 K between the HR and AR face of a Yb:YAG thin disk. Choosing a different laser material with higher thermal conductivity or smaller heat generation would allow for a higher thermal load parameter and enable reaching even higher pulse energies or output powers. Especially for pulsed lasers with a low repetition rate (≤100 Hz), the variation of the pump pulse duration and the pump duty cycle will be an alternative optimization strategy for going far beyond the calculated pulse energy limits.

Table 3. Maximum extractable energy and optimized design parameters for different values of internal loss in resonator

Internal losses L_{int}	1%	4%
Reduced lifetime τ_{ASE}	627 μs	482 μs
Optimized doping concentration N_0	0.36%	1.04%
Thickness h	2.23 mm	0.89 mm
Pump radius r_p	734 mm	61.5 mm
Pump power P_{pump}	9.48 MW	170 kW
Extractable energy	398 J	8.3 J

Data values from Speiser, J., J. Opt. Soc. Am. B **26**(1), 26 (2009).

8. Conclusions

As already stated in the introduction, numerical modeling is an intrinsic part of the design process for thin disk lasers. For the design of cw thin disk lasers of the 10-kW class (per disk), the fundamental modeling questions are solved, but many "engineering" tasks remain concerning optimization of thermal management and mounting design.

Optimizing thin disk lasers with 100 kW per disk as well as thin disk amplifiers with more than 1 J per disk still offer many challenges for improved numerical modeling. Adequate handling of the ASE feedback is still needed and may require a completely different approach. In addition, modeling of the thermal behavior (especially the transient thermal behavior) is not completely described in this case. The task to "dump" 100 kW or even more of ASE power will be a big challenge, especially for the engineering of a compact system.

Appendix A: Material Parameters

Table A.1 shows the material parameters for 9% doped Yb:YAG; all temperatures are in Kelvin. The temperature dependence of the material parameters is shown in Fig. A.1.

The absorption coefficient $\alpha_0(T)$ is given at a wavelength of 941.4 nm. For the absorption calculations, equivalent expressions are evaluated for other wavelengths.

Table A.1. Material parameters for 9 at.% doped Yb:YAG

Emission cross-section	$\sigma_{em,laser}(T) = 0.942 + 35.7843 \cdot \exp(-0.01152 \cdot T) \quad [10^{-20}\,\mathrm{cm}^2]$
Lifetime	$\tau = 951\ \mu s$
Absorption coefficient	$\alpha_0(T) = 9.68 \cdot e^{-0.005 \cdot T} \cdot \left(4.1415 + 0.0062 \cdot (T - 273.15) + 2.83 \cdot 10^{-5} \cdot (T - 273.15)^2\right) [\mathrm{cm}^{-1}]$
Doping concentration	$N_0 = 12.42 \cdot 10^{20}\ \mathrm{cm}^{-3}$
Thermal conductivity	$\lambda_{th}(T) = 6.62 \cdot \left(\frac{204}{T - 96}\right)^{0.439} \quad \left[\frac{\mathrm{W}}{\mathrm{mK}}\right]$
Thermal expansion	$\alpha_{th}(T) = 9.459 \cdot (1 - \exp(-5.23e - 3 \cdot T)) \quad \left[\frac{10^{-6}}{\mathrm{K}}\right]$
Thermo-optical coefficient	$\frac{\partial n}{\partial T} = -3.5 + 0.0548 \cdot T - 5 \cdot 10^{-5} \cdot T^2 \quad \left[\frac{10^{-6}}{\mathrm{K}}\right]$
Young's modulus	$E_{elast} = 284\ \mathrm{GPa}$
Poisson ratio	$\nu = 0.25$

Data derive from Contag, K., *Modellierung und numerische Auslegung des Yb:YAG-Scheibenlasers*, Herbert Utz Verlag, 2002.

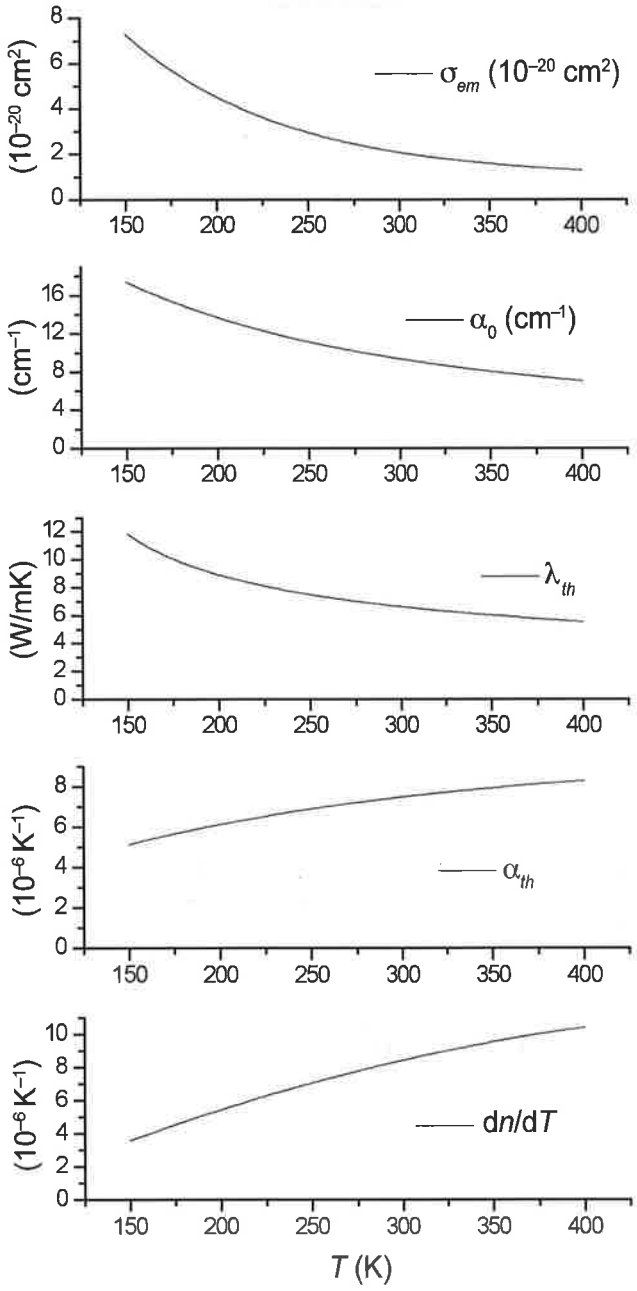

Fig. A.1. Temperature dependence of emission cross-section, absorption coefficient, thermal conductivity, thermal expansion, and thermo-optical coefficient of 9% doped Yb:YAG.

References

[1]Voss, A., Brauch, U., Wittig, K., and Giesen, A., Efficient high-power diode-pumped thin-disc Yb:YAG laser, in Shladov, I., Weissmann, Y., and Kopeika, N., editors, *Proceedings of the 9th Meeting on Optical Engineering in Israel, Tel Aviv, 1994*, vol. 2426, SPIE (1995), p. 501.

[2]Giesen, A., Hügel, H., Voss, A., Wittig, K., Brauch, U, and Opower, H., Appl. Physics B **58**, 365 (1994).

[3]Contag, K., Karszewski, M., Stewen, C., Giesen, A., and Hügel, H., Quantum Electronics **29**(8), 297 (1999).

[4]Contag, K., *Modellierung und numerische Auslegung des Yb:YAG-Scheibenlasers*, Herbert Utz Verlag (2002).

[5]Kemp, A.J., Valentine, G.J., and Burns, D., Prog. Quantum Electron. **28**, 305 (2004).

[6]Baehr, H.D., and Stephan, K., *Wärme- und Stoffübertragung*, Springer (1998).

[7]Larionov, M., *Kontaktierung und Charakterisierung von Kristallen für Scheibenlaser*, Herbert Utz Verlag (2008).

[8]Brauch, U., Giesen, A., Voss, A., and Wittig, K., Laser Amplifying System, U.S. Patent No. 5,553,088 (1996).

[9]Cousins, A.K., IEEE J. Quantum Electron. **28**(4), 1057 (1992).

[10]Contag, K., Brauch, U., Erhard, S., Giesen, A., Johannsen, I., Karszewski, M., Stewen, C., and Voss, A., Simulations of the lasing properties of a thin disk laser combining high output powers with good beam quality, in Farrukh, U.O., and Basu, S., editors: *Modeling and Simulation of Higher-Power Laser Systems IV*, vol. 2989, SPIE (1997), p. 23.

[11]Contag, K., Erhard, S., and Giesen, A., Calculations of optimum design parameters for Yb:YAG thin disk lasers, in Injeyan, H., Keller, U., and Marshall, C., editors: *Advanced Solid State Lasers 2000*, vol. 34, Optical Society of America (2000), p. 124.

[12]Najafi, M., Sepehr, A., Golpaygani, A.H., and Sabbaghzadehet, J., Opt. Commun. **282**, 4109 (2009).

[13]Javadi-Dashcan, M., Hajiesmaeilbaigi, F., Razzaghi, H., Mahdizadeh, M., and Moghadam, M., Opt. Commun. **281**, 4753 (2008).

[14]Kemp, A.J., Maclean, A.J., Hopkins, J.-M., Hastie, J.E., Calvez, S., Dawson, M.D., and Burns, D., J. Mod. Opt. **54**(12), 1669 (2007).

[15]Marion, J., Appl. Phys. Lett. **47**(7), 694 (1985).

[16]Kouznetsov, D., and Bisson, J.-F., J. Opt. Soc. Am. B **25**, 338 (2008).

[17]Stolzenburg, C., Voss, A., Graf, T., Larionov, M., and Giesen, A., Proc. SPIE **6871** (2008).

[18]Kouznetsov, D., Bisson, J.F., Dong, J., and Ueda, K.I., J. Opt. Soc. Am. B **23**, 1074 (2006).

[19]Barnes, N.P., and Walsh, B.M., IEEE J. Quantum Electron. **35**, 101 (1999).

[20]Lowenthal, D.D., and Eggleston, J.M., IEEE J. Quantum Electron. **22**, 1165 (1986).

[21]Okuda, M.J., and Shaw, Appl. Phys. B **54**, 506 (1992).

[22]Sasaki, A., Ueda, K.-I., Takuma, H., and Kasuya, K., J. Appl. Phys. **65**, 231 (1989).

[23]Speiser, J., and Giesen, A., Proc. SPIE **6871** (2008).

[24]Speiser, J., Laser Physics **19**(2), 274 (2009).

[25]Speiser, J., J. Opt. Soc. Am. B **26**(1), 26 (2009).